Instability of radially spreading extensional flows Part II: Theoretical analysis

ROIY SAYAG[1,2]†, AND M. GRAE WORSTER[3]

[1]Dept. of Environmental Physics, Blaustein Institutes for Desert Research, Ben-Gurion University of the Negev, Sede Boqer Campus, 8499000, Israel

[2]Dept. of Mechanical Engineering, Ben-Gurion University of the Negev, Beer-Sheva 8410501, Israel

[3]Dept. of Applied Mathematics and Theoretical Physics, University of Cambridge, Cambridge CB3 0WA, UK

(Received ?; revised ?; accepted ?. - To be entered by editorial office)

The interface of a strain–rate–softening fluid that displaces a low–viscosity fluid in a circular geometry with negligible drag can develop finger–like patterns separated by regions in which the fluid appears to be torn apart. Such patterns were observed and explored experimentally in part I using polymeric solutions. They do not occur when the viscosity of the displacing fluid is constant, or when the displacing fluid has no–slip conditions along its boundaries. We investigate theoretically the formation of tongues at the interface of an axisymmetric initial state. We show that finger–like patterns can emerge when circular interfaces of strain–rate–softening fluids displace low–viscosity fluids between stress–free boundaries. The instability, which is fundamentally different from the classical Saffman–Taylor viscous fingering, is driven by the tension that builds up along the circular front of the propagating fluid. That destabilising tension is a geometrical consequence and is present independently of the nonlinear properties of the fluid. Shear stresses stabilise the growth either along extended circumferential streamlines or through a street of vortices. However, such stabilising processes become weaker, thereby allowing the instability to develop, the more strain–rate softening the fluid is. The theoretical model that we present predicts the main experimental observations made in part I. In particular, the patterns we predict using linear–stability theory are consistent with the strongly nonlinear experimental patterns. Our model depends on a single dimensionless number representing the power–law exponent, which implies that the instability we describe could arise in any extensional flow of strain–rate–softening material, ranging from suspensions that rupture in squeeze experiments to rifts formed in ice shelves.

1. Introduction

Interfaces between fluids that displace other fluids in quasi–two dimensional geometries are common in various natural and industrial systems. In some settings, such interfaces can maintain a smooth circular or planar shape, but in others they can develop fingering instabilities, which can be beneficial to some processes and detrimental to others. Therefore, predicting the stability of such interfaces and controlling it is of major interest.

A large class of interfacial–stability problems, known as viscous fingering, involves

† Email address for correspondence: roiy@bgu.ac.il

flows that are dominated by shear, typically due to the traction imposed by confining solid boundaries. In these shear–dominated flows in a uniform gap, it is established that the interface is stable when the displacing fluid is more viscous (less mobile), either in a system of Newtonian fluids (e.g., Saffman & Taylor 1958; Homsy 1987; Wooding & Morelseytoux 1976; Paterson 1981; Cardoso & Woods 1995; Jha *et al.* 2011), or when at least one of the fluids are complex (e.g., Coussot 1999; Lindner *et al.* 2000*a*; Kondic *et al.* 1998; Zhao & Maher 1993). The development of instability in these systems is primarily because the magnitude of the driving pressure gradient is larger in the displaced fluid than in the displacing fluid, as described in more detail in Part I.

Another important factor for the stability of shear–dominated flows is the flow geometry. Particularly, for a constant–flux source, Newtonian flows in a circular geometry tend to be more stable than flows in a linear geometry (e.g., Paterson 1981) because the velocity of circular interfaces declines with time and circumferential stretching tends to push perturbations to lower wavenumbers. In the case of strain–rate–softening fluids, an axisymmetric flow configuration may appear prone to an instability in a single fluid phase. This is because the declining strain rate with radius leads to monotonically growing viscosity, or declining mobility, with radius, which implies that any ring of fluid within such flows is like an interface between an inner less–viscous fluid and an outer more–viscous fluid. Although there is no viscosity jump across such fluid rings and they behave as rather smeared interfaces, one might anticipate that instability could still occur as it does in miscible Newtonian fluids (Paterson 1985; Manickam & Homsy 1993; Holloway & de Bruyn 2005). However, viscous fingering in displacing strain–rate–softening fluids was not observed thus far. Similar axisymmetric flows of strain–rate softening fluids were also studied using viscous gravity currents that propagate into low–viscosity fluids over a horizontal substrate. Such flows have mixed boundary conditions of no–slip along their base and no–stress along their free surface due to the absence of confinement. Here too, despite a radially increasing viscosity within the strain–rate–softening displacing fluids, no fingering was observed (Sayag & Worster 2013).

In another class of problems, which form the focus of this paper, the fluids have free top and bottom surfaces along which traction is negligible and the circular flow is dominated by extension rather than by shear. In this case evidence shows that unique finger–like patterns can arise, with the fluid appearing to be torn apart, when the displacing fluid is strain–rate softening. For example, ice shelves deform like strain–rate–softening fluids (Glen 1955) under negligible traction, as they spread over the ocean. When ice shelves are free from lateral confinement, finger–like patterns can emerge normal to the shelf front, separated by deep rifts, reminiscent of tears (rips) that cut through the entire ice thickness (Hughes 1983; Doake & Vaughan 1991; Bassis *et al.* 2008; Borstad *et al.* 2017). Similarly tear–like patterns emerge when pastes squeezed by parallel disks emerge outside of the rim of the disks into a region that is unconfined where no external stress is applied (Roussel *et al.* 2006; Mascia *et al.* 2006). These patterns are potentially related to the migration of the liquid phase within the pastes as they spread. In contrast, the interface remains stable in similar flows of Newtonian displacing fluids, such as viscous gravity currents that spread under no traction (Pegler & Worster 2012).

In part I of this study (Sayag & Worster 2019) we present a laboratory study in which thin films of strain–rate softening fluids displacing ambient low–viscosity fluids developed tearing patterns. The gravity–driven displacing fluid evolved in circular geometry under spatially mixed boundary conditions: at radii $r < r_G$ the flow was under no–slip basal conditions, while for $r > r_G$ no–stress basal conditions were imposed, where the transition position r_G was fixed in time. The top free surface of the displacing fluid was under no–stress conditions uniformly. We found that an initially circular front of the displacing

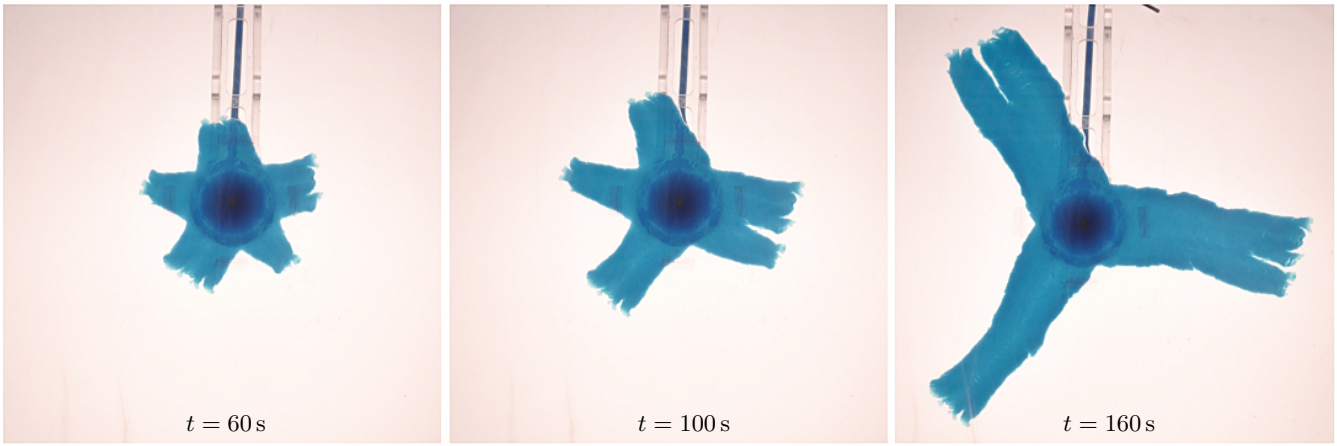

FIGURE 1. Selected plan view snapshots from a laboratory experiment with constant source flux ($Q = 2.64$ gm/cm^3), showing polymer solution (blue) displacing a denser salt solution (transparent) in circular geometry (Sayag & Worster 2019).

fluid became unstable near r_G and developed tongues that moved as solid blocks (Fig. 1), similar to the movement of floating ice tongues (e.g. Holdsworth 1983) or of foam under wall slip (Lindner *et al.* 2000*b*). The tips of the tears at r_G were sharp, reminiscent of fracture tips. As the tongues grew longer, some of those tips were advected with the flow and, as they did, they closed down by the joining of adjacent tongues into wider ones. Consequently, the number of tongues declined with time (Fig. 1) in patterns that emerged consistently over a wide range of fluxes of the displacing fluid (Sayag & Worster 2019). Such an inverse cascade of the number of tears or the tongues in between appears also to characterise the patterns observed in squeezed pastes (Mascia *et al.* 2006) and in fractured thin elastic plates (Vandenberghe *et al.* 2013; Vermorel *et al.* 2010).

In this part II of the study of instability of radially–spreading extensional flows, we analyse theoretically the laboratory experiments that were presented in part I (Sayag & Worster 2019). We show that the instability that leads to the formation of tongues has an entirely different mechanism than the classical Saffman–Taylor viscous fingering. In particular, it is a consequence of the unique configuration of circular geometry combined with free–slip boundary conditions and strain–rate–softening displacing fluid. Although the displacing fluid in those experiments was viscoelastic, they were performed at small Deborah and Reynolds numbers (Sayag & Worster 2019), implying that the leading–order deformation was viscous and that the flow was inertialess. Under these conditions, we develop a general mathematical model for power–law fluids that consists of the major physical and geometrical components of the laboratory experiments (§2). We use linear–stability theory to explore the instability of axiysymmetric solutions and the possible development of fingers, and investigate several asymptotic limits of that model to validate numerical results (§3) and to elucidate the underlying physical mechanism of the instability (§4). We then focus on the consistency of the model predictions with the experimental measurements (§5) reported in Sayag & Worster (2019).

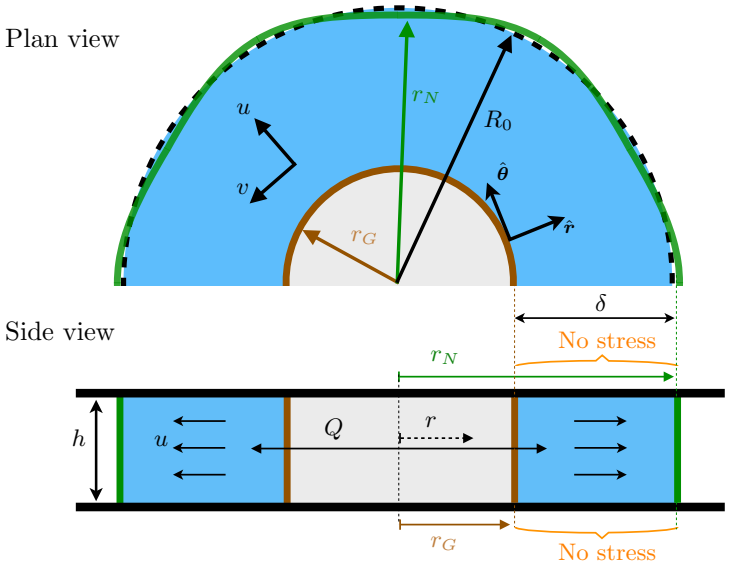

FIGURE 2. Diagram of the flow geometry considered in the mathematical model

2. The mathematical model

In order to understand our two major experimental observations – that the initially circular interface becomes unstable as it begins to float, and that the number of emerging tongues declines with time (Sayag & Worster 2019), we develop a relatively simple model that captures the major physical and geometrical components of the system.

We consider the flow in an annular layer of fluid that emerges from a fixed inner radius at r_G, representing the position where the fluid begins to float, and that has an outer radius $r_N(\theta, t)$, representing the leading interface of the displacing fluid layer, that evolves with time and can vary with azimuth (Fig. 2). Based on the experimental observations that variations in the thickness of the floating fluid layer were not significant, we assume that the layer has a uniform thickness h. Traction is absent along the top and bottom surfaces of the propagating fluid so that the horizontal flow is vertically uniform. This situation is analogous to the flow inside a Hele–Shaw cell with a uniform gap but with no–stress conditions along the rigid boundaries. The displacing fluid is discharged axisymmetrically at a constant flux Q from a cylindrical source of radius r_G, and the flow throughout the domain is inertialess ($Re \ll 1$). We assume that the displacing fluid is purely viscous, in light of the evidence presented in part i that the experiments were performed in small Deborah number ($\mathrm{De} \ll 1$) and evidence from other extensional flows (Trouton ratio) or shear dominated flows (normal to shear stress ratio) that the elastic behaviour of the same fluid becomes dominant at higher deformation rates than those used in part i (Sayag & Worster 2019).

Mathematically we consider the two–dimensional Stokes flow of a power–law fluid

governed by the equations

$$\left.\begin{aligned}\boldsymbol{\nabla}\cdot\boldsymbol{\sigma}&=\boldsymbol{0}\\ \boldsymbol{\nabla}\cdot\boldsymbol{u}&=0\end{aligned}\right\}\quad \text{in } r_G<r<r_N, \tag{2.1a}$$

$$\int_0^{2\pi}\int_{r_G}^{r_N} r\;dr\;d\theta=\frac{Qt}{h}, \tag{2.1b}$$

$$\dot{r}_N=u(r_N), \tag{2.1c}$$

where $\boldsymbol{u}=u\hat{\boldsymbol{r}}+v\hat{\boldsymbol{\theta}}$ is the plane velocity field with radial and azimuthal components u and v respectively, $\dot{r}_N=\partial r_N/\partial t$, and $\boldsymbol{\sigma}$ is the full two–dimensional stress tensor.

The viscous deformation of the displacing fluid in part i is consistent with a power–law fluid of both shear and extensional thinning for a wide range of strain rates with an approximately similar exponent. As the deformation rate tends to zero the fluid may unyield or have a bounded viscosity. Here we are interested in exploring the dynamics near the emergence of the tongues, where the propagating front is not far from the inner boundary. In this range, the experimental setting suggests that the deformation rate is consistent with the power–law behaviour of the fluid and that elasticity doesn't dominate. Along the developed tongues, further away radially from the inner boundary and the tip of the tears where the tongues emerge, the fluid may unyield or have a much larger viscosity than in the region of interest. These evidences encourage us to use the simpler power–law model as a deformation law with the notion that the leading–order qualitative behaviour is captured. Moreover, the viscosity singularity of a strain–rate–softening power-law fluid at zero strain rate is reminiscent of a yield stress. Therefore, we consider a two dimensional stress tensor of a generalised Newtonian fluid $\boldsymbol{\sigma}=-p\boldsymbol{I}+2\mu\boldsymbol{e}$, where p is the pressure field, $\boldsymbol{e}=\frac{1}{2}\left(\nabla\boldsymbol{u}+\nabla\boldsymbol{u}^T\right)$ is the rate–of–strain tensor, and μ is the strain–rate–dependent viscosity of a power–law fluid, given by

$$\mu=m e_{II}^{\frac{1}{2}\left(\frac{1}{n}-1\right)}, \tag{2.2}$$

with $e_{II}\equiv\frac{1}{2}\boldsymbol{e}:\boldsymbol{e}$ an invariant of the tensor $\boldsymbol{e}$, n is a dimensionless, constant material property and m is a constant consistency factor. This model represents strain–rate softening material when $n>1$, a strain–rate hardening material when $0<n<1$, and a Newtonian fluid when $n=1$. Note that in some literature, n is defined as the inverse of what is used here. Our choice is motivated by the common usage in glaciological studies. Equations (2.1) are respectively the momentum balance, local mass balance, global mass balance, and a kinematic interfacial condition that the velocity of the front is equal to the material radial velocity at the front. The boundary conditions at the inner and outer radii are

$$u=\frac{Q}{2\pi hr},\quad v=0\ \text{ at }\ r=r_G, \tag{2.3a}$$

$$\hat{\boldsymbol{n}}\cdot\boldsymbol{\sigma}\cdot\hat{\boldsymbol{t}}=0,\quad \hat{\boldsymbol{n}}\cdot\boldsymbol{\sigma}\cdot\hat{\boldsymbol{n}}=0\ \text{ at }\ r=r_N(\theta,t), \tag{2.3b}$$

where

$$\hat{\boldsymbol{n}}=\frac{\hat{\boldsymbol{r}}-\dfrac{r'_N}{r_N}\hat{\boldsymbol{\theta}}}{\sqrt{1+\left(\dfrac{r'_N}{r_N}\right)^2}},\qquad \hat{\boldsymbol{t}}=\frac{\dfrac{r'_N}{r_N}\hat{\boldsymbol{r}}+\hat{\boldsymbol{\theta}}}{\sqrt{1+\left(\dfrac{r'_N}{r_N}\right)^2}} \tag{2.4}$$

are respectively the normal and tangential unit vectors at the moving interface r_N, with $r'_N\equiv\partial r_N/\partial\theta$. Conditions (2.3) represent the uniform injection velocity and no slip at

the inner radius r_G, and that the outer interface is stress–free. We nondimensionalise (2.1-2.3) letting

$$\begin{aligned} r &= r_G\tilde{r}, & t &= \mathcal{T}\tilde{t}, & u &= \mathcal{U}\tilde{u}, \\ v &= \mathcal{U}\tilde{v}, & p &= \mathcal{P}\tilde{p}, & \mu &= \mathcal{M}\tilde{\mu}, \end{aligned} \tag{2.5}$$

where a tilde denotes a dimensionless variable, and

$$\mathcal{U} \equiv \frac{Q}{2\pi h r_G}, \quad \mathcal{T} \equiv \frac{r_G}{\mathcal{U}}, \quad \mathcal{M} \equiv m\mathcal{T}^{\left(1-\frac{1}{n}\right)}, \quad \mathcal{P} \equiv \frac{\mathcal{M}}{\mathcal{T}} \tag{2.6}$$

are characteristic scales for the velocity, time, viscosity and pressure, respectively. Substituting and removing tildes leads to the dimensionless equations

$$\left.\begin{aligned} \boldsymbol{\nabla}\cdot(2\mu\boldsymbol{e}) &= \boldsymbol{\nabla}p \\ \boldsymbol{\nabla}\cdot\boldsymbol{u} &= 0 \end{aligned}\right\} \quad \text{in } 1 < r < R(\theta,t), \tag{2.7a}$$

$$\int_0^{2\pi}\int_1^R r\; dr\; d\theta = 2\pi t, \tag{2.7b}$$

$$\dot{R} = u(R), \tag{2.7c}$$

where $R(\theta,t) \equiv r_N(\theta,t)/r_G$ and $\dot{R} = \partial R/\partial t$, to the dimensionless viscosity

$$\mu = e_{II}^{\frac{1}{2}\left(\frac{1}{n}-1\right)}, \tag{2.8}$$

and to the dimensionless boundary conditions

$$u = 1, \quad v = 0 \qquad \text{at } r = 1, \tag{2.9a}$$

$$\left.\begin{aligned} \sigma_{r\theta} - \frac{R'}{R}\left(\sigma_{\theta\theta}-\sigma_{rr}\right) - \left(\frac{R'}{R}\right)^2\sigma_{r\theta} &= 0 \\ \sigma_{rr} - 2\frac{R'}{R}\sigma_{r\theta} + \left(\frac{R'}{R}\right)^2\sigma_{\theta\theta} &= 0 \end{aligned}\right\} \quad \text{at } r = R(\theta,t), \tag{2.9b}$$

where $R' = \dfrac{\partial R}{\partial\theta}$ and where the dimensionless stress tensor is $\boldsymbol{\sigma} = -p\boldsymbol{I} + 2\mu\boldsymbol{e}$. Consequently, equations (2.7, 2.9) involve a single dimensionless parameter n that enters the constitutive equation through the viscosity function μ.

3. Linear stability analysis

We investigate the temporal stability of the front $r = r_N(\theta,t)$ to small perturbations with respect to an axisymmetric base state.

3.1. *The base state*

We look for an axisymmetric solution to (2.7, 2.9) in which

$$u = u_0(r), \quad v = 0, \quad p = p_0(r), \quad R = R_0(t). \tag{3.1}$$

Consequently, the boundary conditions at the front R_0 (2.3*b*) simplify to

$$\sigma_{0r\theta} = \sigma_{0rr} = 0. \tag{3.2}$$

The solution, which we refer to as the *base state*, is given by the radial flow from a cylindrical source from which we can determine that

$$u_0 = \frac{1}{r}, \qquad v_0 = 0, \quad R_0 = \sqrt{1+2t}, \tag{3.3a}$$

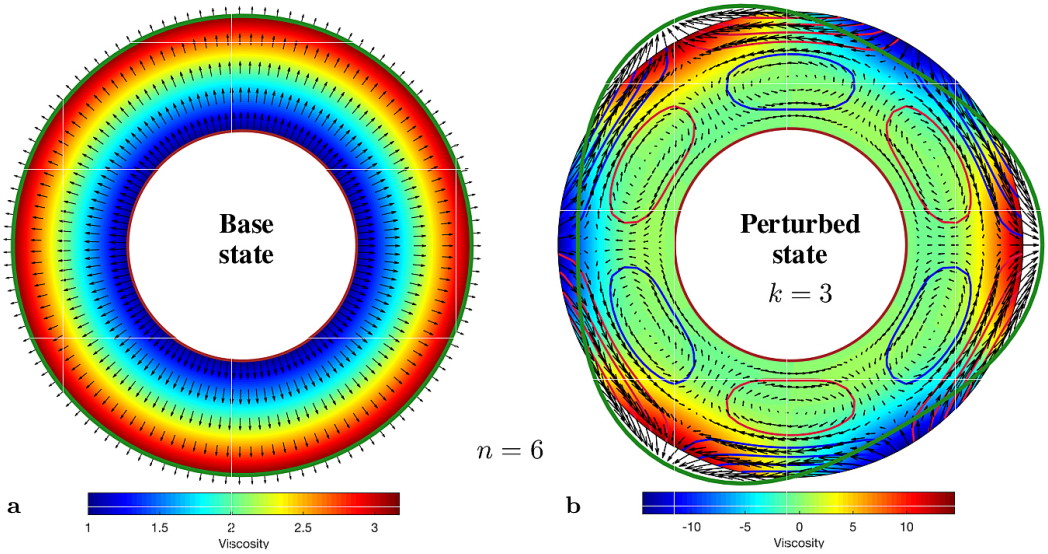

FIGURE 3. The base state and a perturbed state for $n = 6$, $R_0 = 2$. (a) The base state is axisymmetric with radially growing viscosity μ_0 (color). (b) The perturbation flow for $k = 3$, showing the perturbation viscosity (color), velocity field (arrows) and streamlines (blue and red curves), where $\mathcal{G} = 0.1$. In both panels (▬) marks the inner boundary r_G, and (▬) marks the leading front r_N.

so that

$$\boldsymbol{e}_0 = \frac{1}{r^2}\begin{pmatrix} -1 & 0 \\ 0 & 1 \end{pmatrix}, \tag{3.3b}$$

$$\mu_0 = r^{2(1-1/n)}, \qquad \frac{\partial p_0}{\partial r} = -\frac{2}{r^2}\frac{\partial \mu_0}{\partial r}. \tag{3.3c}$$

Therefore, strain rates decline inversely with the square of the radius, which implies that the viscosity of a strain–rate softening fluid ($n > 1$) increases radially (Fig. 3a), while that of a strain–rate hardening material ($0 < n < 1$) declines radially. Note that equations (3.3*b*) and (3.3*c*) imply that

$$p_0 = 2(n-1)r^{-2/n} - 2nR_0^{-2/n}, \tag{3.4a}$$

$$\sigma_{0rr} = -2n\left(r^{-2/n} - R_0^{-2/n}\right), \tag{3.4b}$$

$$\sigma_{0\theta\theta} = -2n\left(r^{-2/n} - R_0^{-2/n}\right) + 4r^{-2/n}. \tag{3.4c}$$

3.2. *Evolution of small perturbations.*

We next apply a harmonic perturbation to the base state having an azimuthal wavenumber k, and investigate its linear stability. The full fields have the form

$$\boldsymbol{F} = \boldsymbol{F}_0(r) + \boldsymbol{F}_1(r,\theta,t), \tag{3.5a}$$

$$R = R_0(t) + R_1(\theta,t), \tag{3.5b}$$

where the subscripts 0,1 denote respectively the base state and the perturbation field, $\boldsymbol{F_0} \equiv (u_0, v_0, p_0, \boldsymbol{e}_0)$, $\boldsymbol{F_1} \equiv (u_1, v_1, p_1, \boldsymbol{e}_1)$. The geometric perturbation is $R_1 = \varepsilon e^{ik\theta+\mathcal{G}t}$,

where $\varepsilon \ll 1$ is the perturbation amplitude, k is the circumferential wavenumber, $\mathcal{G}$ is the growthrate, and $\boldsymbol{F_1}/R_1$ is a function of r of order of unity. The perturbation strain–rate components are

$$e_{1rr} = \frac{\partial u_1}{\partial r}, \tag{3.6a}$$

$$e_{1\theta\theta} = \frac{1}{r}\frac{\partial v_1}{\partial \theta} + \frac{u_1}{r}, \tag{3.6b}$$

$$e_{1r\theta} = \frac{1}{2}\left(\frac{1}{r}\frac{\partial u_1}{\partial \theta} + \frac{\partial v_1}{\partial r} - \frac{v_1}{r}\right). \tag{3.6c}$$

The corresponding strain–rate invariant becomes

$$e_{II} = \frac{1}{2}\left(\boldsymbol{e}_0 + \boldsymbol{e}_1\right) : \left(\boldsymbol{e}_0 + \boldsymbol{e}_1\right) = \frac{1}{2}\boldsymbol{e}_0 : \boldsymbol{e}_0 + \boldsymbol{e}_0 : \boldsymbol{e}_1 \tag{3.7}$$

to leading order. If we denote $e_{II_0} \equiv \frac{1}{2}\boldsymbol{e}_0 : \boldsymbol{e}_0 = e_{0rr}^2 = r^{-4}$ and $e_{II_1} \equiv \boldsymbol{e}_0 : \boldsymbol{e}_1 = 2e_{0rr}e_{1rr} = -2e_{1rr}r^{-2}$ then Taylor expansion of the viscosity implies that to leading order

$$\begin{aligned}\mu\left(e_{II}\right) = \mu\left(e_{II_0} + e_{II_1}\right) &= \left(e_{II_0} + e_{II_1}\right)^{\frac{1}{2}\left(\frac{1}{n}-1\right)} \\ &= e_{II_0}^{\frac{1}{2}\left(\frac{1}{n}-1\right)} + e_{II_1}\frac{1}{2}\left(\frac{1}{n}-1\right)\frac{e_{II_0}^{\frac{1}{2}\left(\frac{1}{n}-1\right)}}{e_{II_0}} \\ &= \mu_0 + \mu_1,\end{aligned}$$

where the perturbation viscosity is

$$\mu_1 = \left(1 - \frac{1}{n}\right)\mu_0 r^2 e_{1rr}. \tag{3.8}$$

Therefore, the decomposed stress field is

$$\begin{aligned}\boldsymbol{\sigma} = \boldsymbol{\sigma}_0 + \boldsymbol{\sigma}_1 &= -(p_0 + p_1)\boldsymbol{I} + 2\left(\mu_0 + \mu_1\right)\left(\boldsymbol{e}_0 + \boldsymbol{e}_1\right) \\ &= -p_0\boldsymbol{I} + 2\mu_0\boldsymbol{e_0} + \left(-p_1\boldsymbol{I} + 2\mu_0\boldsymbol{e}_1 + 2\mu_1\boldsymbol{e}_0\right),\end{aligned}$$

resulting in perturbation stress components

$$\sigma_{1rr} = -p_1 + \frac{2\mu_0}{n}e_{1rr}, \tag{3.9a}$$

$$\sigma_{1\theta\theta} = -p_1 + \frac{2\mu_0}{n}e_{1\theta\theta}, \tag{3.9b}$$

$$\sigma_{1r\theta} = 2\mu_0 e_{1r\theta}. \tag{3.9c}$$

Therefore, substituting the perturbed fields in (2.7a), the order ε force–balance equations are

$$\frac{1}{n}\left[\frac{\partial}{\partial r}\left(2\mu_0 e_{1rr}\right) + \frac{4}{r}\mu_0 e_{1rr}\right] + \frac{2}{r}\frac{\partial}{\partial \theta}\left(\mu_0 e_{1r\theta}\right) = \frac{\partial p_1}{\partial r}, \tag{3.10a}$$

$$\frac{1}{n}\left[\frac{2}{r}\frac{\partial}{\partial \theta}\left(\mu_0 e_{1\theta\theta}\right)\right] + \frac{4}{r}\mu_0 e_{1r\theta} + \frac{\partial}{\partial r}\left(2\mu_0 e_{1r\theta}\right) = \frac{1}{r}\frac{\partial p_1}{\partial \theta}, \tag{3.10b}$$

while the continuity equation in (2.7a) can be expressed as

$$e_{1rr} + e_{1\theta\theta} = 0. \tag{3.10c}$$

It is interesting to note that n does not appear additively in a coefficient proportional to $n-1$ but rather multiplicatively in coefficients proportional to $1/n$. This is an indication

that non–Newtonian effects do not introduce new qualitative influences but rather modify physical influences quantitatively. We return to this point in §3.4 below.

Following a similar substitution in (2.7*b*) the linear terms in ε

$$\int_0^{2\pi} e^{ik\theta}\, d\theta = 0$$

imply that the wavenumber k is integer, as expected from the requirement of periodicity around a circle. The kinematic condition (2.7*c*) gives

$$\begin{aligned}\mathcal{G} &= \left(\frac{\partial u_0}{\partial r} + \frac{u_1}{R_1}\right)\Bigg|_{r=R_0} \\ &= -\frac{1}{R_0^2} + \frac{u_1}{R_1}\Bigg|_{r=R_0},\end{aligned} \tag{3.11}$$

to leading order. The first term in this expression is always negative and therefore suppresses the perturbation growth and stabilizes the flow independently of the constitutive model. This is a reflection of mass conservation, since the azimuthal straining of the base flow $e_{0\theta\theta}$ is always and everywhere positive, and is simultaneous with radial compression $e_{0rr} = -e_{0\theta\theta} < 0$ (3.10*c*). Thus, the base flow radial velocity of the front diminishes with r in order to compensate for the areal expansion with radius, thereby tending to keep the front axisymmetric.

The conditions at the inner boundary are

$$u_1 = 0, \quad \frac{\partial u_1}{\partial r} = 0 \ \text{ at } \ r = 1, \tag{3.12a}$$

where continuity was used to derive the last equation from the no–slip condition. The order ε stress conditions (2.3*b*) at the front R simplify to

$$\left.\begin{aligned}\sigma_{1r\theta} &= \frac{\partial R}{\partial \theta}\frac{\sigma_{0\theta\theta} - \sigma_{0rr}}{R_0}, \\ \sigma_{rr} &= 0\end{aligned}\right\} \quad \text{at } r = R. \tag{3.12b}$$

Expanding further around R_0 we find that

$$\left.\begin{aligned}e_{1r\theta} &= \frac{2}{R_0^3}\frac{\partial R_1}{\partial \theta}, \\ p_1 &= \frac{2\mu_0}{n}e_{1rr} + \frac{4\mu_0}{R_0^3}R_1\end{aligned}\right\} \quad \text{at } r = R_0. \tag{3.12c}$$

3.3. *Numerical solution of the perturbation equations*

We solved equations (3.10) together with the boundary conditions (3.12) using MATLAB bvp4c. In this method, R_0, n and k are treated as specified parameters and the solver computes the perturbation velocity and pressure fields. Having the solution for the perturbation velocity field (e.g., Fig. 3b) we evaluate the radial perturbation velocity at the base–state front and then the growthrate $\mathcal{G}$ using (3.11).

Repeating this computation for a range of the parameters k, n, and R_0, we find a range of unstable modes, which we describe through the neutral–stability curves ($\mathcal{G} = 0$) for each wavenumber k in the $n - \delta$ space, where $\delta \equiv R_0 - 1$ represents the width of the base–state annular shape (Fig. 4a). Neutral curves $n(\delta)$ are shown for some specified values of k, and the envelope of these curves gives a global neutral curve. We find that unstable modes, in which circular fronts break down into fingered fronts can emerge

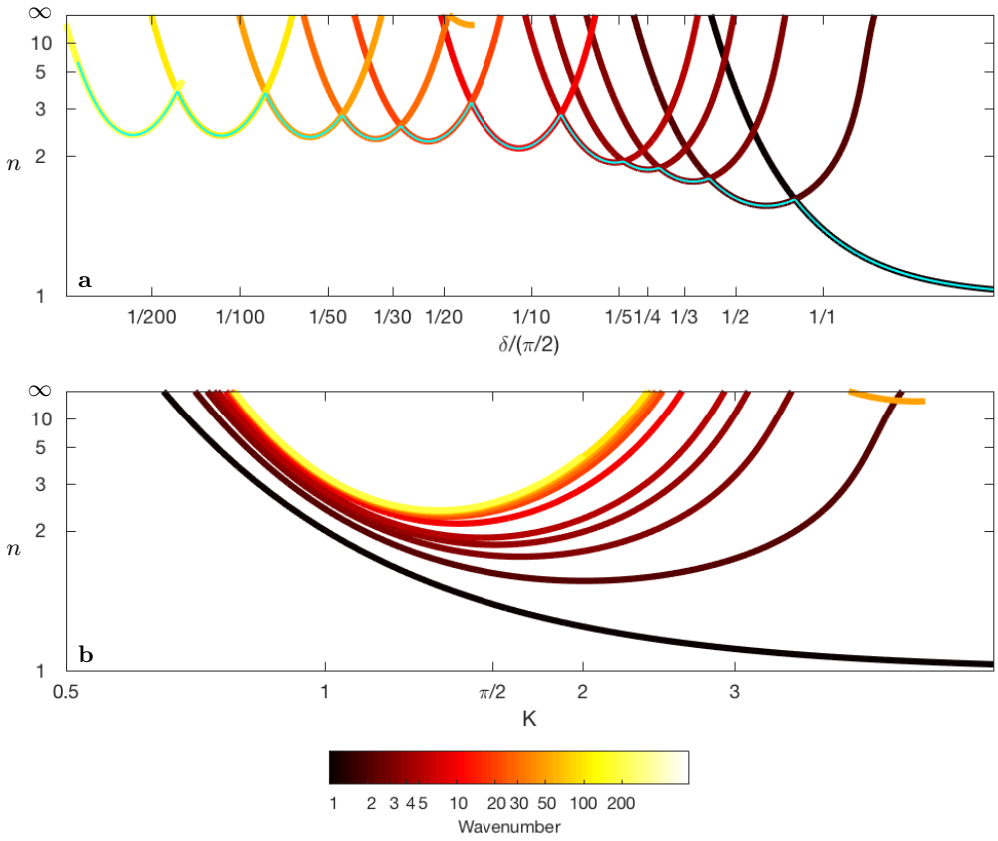

FIGURE 4. (**a**) Results of the stability analysis, showing the neutral curves (color) of the set of wavenumbers $k = 1, 2, 3, 4, 5, 10, 20, 30, 50, 100, 200$ as a function of the power–law exponent n and of the normalised thickness of the annular layer of fluid $\delta/(\pi/2)$. The unstable region is always above the neutral curves. The envelope of these neutral curve is marked by ▬. When more modes are included (e.g., Fig. 5) that envelope converges to a global neutral curve, which is flatter at the left edge (smaller δ). (**b**) The same modal neutral curves presented in panel (a), but as a function of the dimensionless quantity $K \equiv k\delta$ converge with the growth of k to a universal neutral curve near $K \sim \pi/2$. Modes with $n < 1$ are always stable and therefore not shown.

in fluids that are sufficiently strain–rate softening ($n > 1$). Specifically, each neutral–stability curve in the $n - \delta$ space corresponding to a particular mode $k > 1$ has a general U shape that encloses an unstable domain between some finite $n > 1$ and $n \to \infty$. The $k = 1$ neutral curve is unique, since it is open and asymptotically converges to $n = 1$ as $\delta \to \infty$. The minimum of each of the $k > 1$ curves coincides approximately with the base–state width $\delta/(\pi/2) = 1/k$. Therefore, plotting the same neutral curves versus $K \equiv \delta k$ (Fig. 4b) results in a series of neutral curves that converge as $k \to \infty$ to a universal curve whose minimum is approximately at $K = \pi/2$. This universality with respect to K motivates the development of a simpler model for the perturbation field that depends on two parameters n, K rather than the present triple n, k, δ, which we investigate thoroughly in §3.5.

The neutral curves in Fig. 4a intersect and form a global domain of unstable modes out of a small set of wavenumbers. To identify the most–unstable mode for each n and

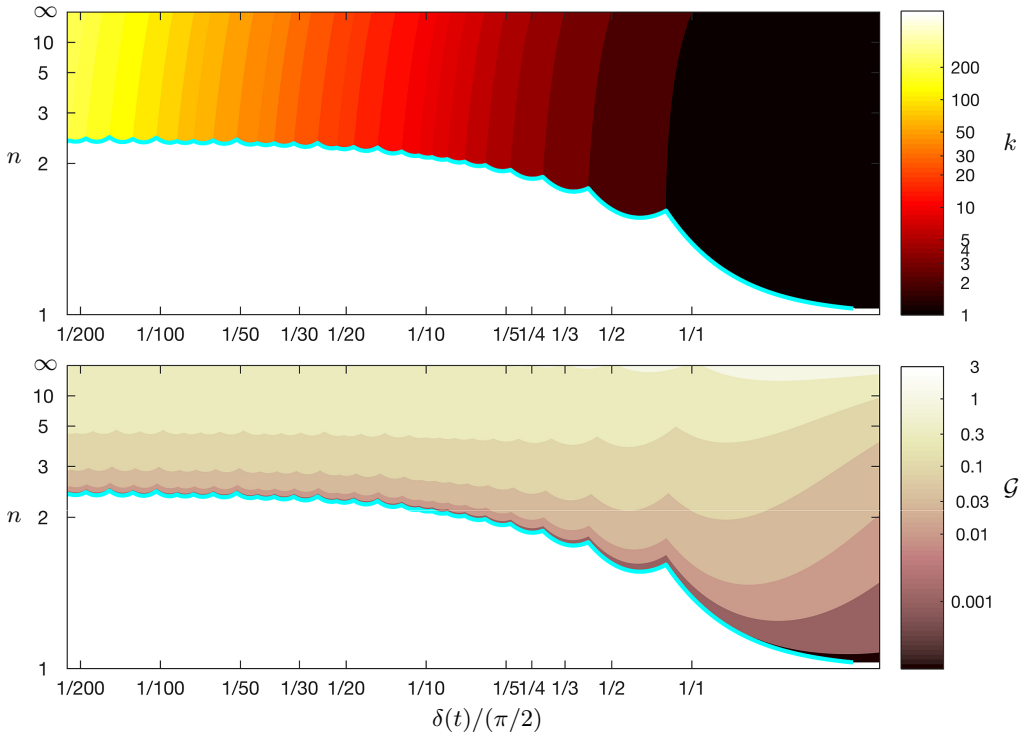

FIGURE 5. Results of the stability analysis, showing the most–unstable wavenumbers k (**a**) and the corresponding growthrates (**b**) as a function of the power–law exponent n and of the thickness of the annular layer of fluid $\delta/(\pi/2)$, among a denser (but not complete) set of wavenumbers than that shown in Fig. 4. Therefore, the envelope of these neutral curve (▬) is more similar to the global neutral curve than the one shown in Fig. 4. Modes with $n < 1$ are stable and therefore not shown.

δ, we compare the growthrates among a finite though more dense set of modes (Fig. 5a). Consequently we find that the most–unstable wavenumbers depend only weakly on n. In addition, the corresponding growthrates depend only weakly on δ, but grow with n (Fig. 5b).

Considering the details of the perturbation flow, we find that it can vary substantially between different modes, and between fluids that are strain–rate softening and strain–rate hardening (Fig. 6). For strain–rate–softening fluids, the perturbation viscosity is positive where the perturbed front has a forward bulge ($R_1 > 0$) and negative along frontal depressions ($R_1 < 0$), implying that the fluid in bulges is stiffer while in depressions it is softer ($n > 1$, Fig. 6b). In the case of strain–rate–hardening fluids, the viscosity distribution is opposite so that the fluid in forward bulges is more mobile ($n < 1$, Fig. 6a). Unlike the base–state flow, which is purely radial, the secondary flow involves a significant azimuthal component. Particularly, there are qualitatively two flow patterns – a converging flow mode in which mass is carried from frontal depressions to bulges (open streamlines), and a vortex–flow mode (closed streamlines) that consists of vortices that are centered at the depression–bulge boundaries and rotate such that their radial component is negative in the center of bulges and positive in the center of depressions. The two flow patterns can coexist (Fig. 6) and the total vortex–covered area grows with wavenumber and with the inverse of n, so that a growing volume of fluid is trapped within vortices while flow

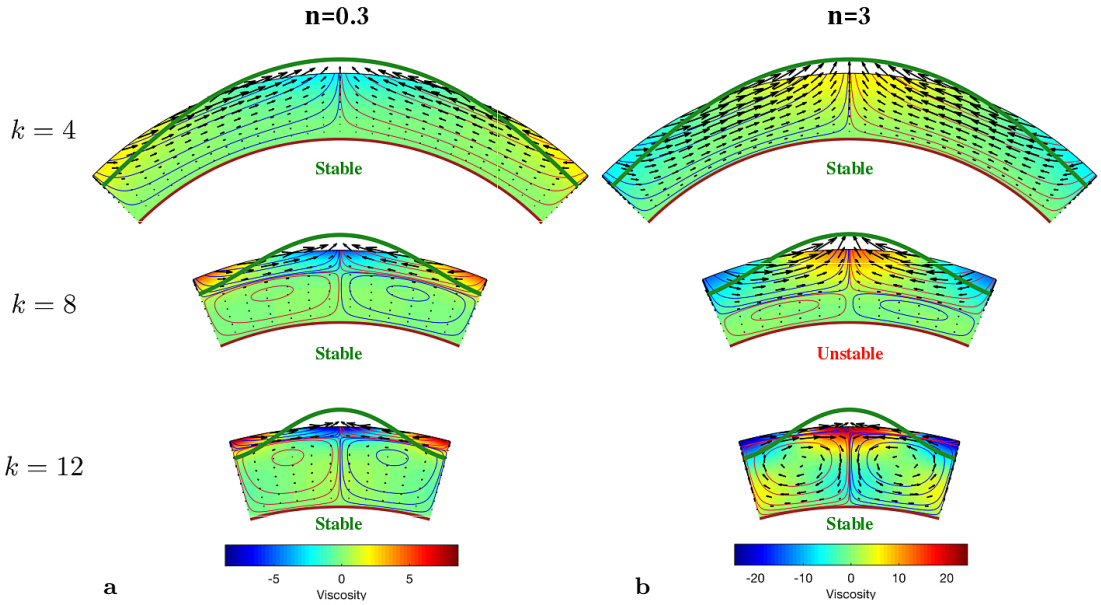

FIGURE 6. One–wavelength sections of the two dimensional flow for $k = 4, 8, 12$ ($R_0 = 1.23$) and for $n = 0.3$ (left column) and $n = 3$ (right column), showing the perturbation velocity field ($\rightarrow$), streamlines (— (clockwise) and — (counter clockwise) curves), perturbed front (▬) and viscosity field (color). All modes are stable apart of the $k = 8, n = 3$ mode. The specific growthrates are (from low to high wavenumbers) $\mathcal{G} \approx -0.54, -0.53, -0.55$ ($n = 0.3$) and $\mathcal{G} \approx -0.03, +0.1, -0.41$ ($n = 3$). Streamlines absolute value: 0.002, 0.016, 0.064, 0.256, 0.512.

convergence into bulges persists over increasingly smaller regions. The nature of these vortices is discussed in more details in §4.4.2.

To validate the numerical results and investigate the mechanism of the instability, we develop explicit solutions in several asymptotic limits in the following sections.

3.4. *Asymptotic solutions: The Newtonian–fluid limit*

In the Newtonian limit ($n = 1$)

$$\mu_0 = 1, \tag{3.13}$$

so that the perturbation equations simplify to

$$2\frac{\partial e_{1rr}}{\partial r} + \frac{4}{r}e_{1rr} + \frac{2}{r}\frac{\partial e_{1r\theta}}{\partial \theta} = \frac{\partial p_1}{\partial r}, \tag{3.14a}$$

$$\frac{2}{r}\frac{\partial e_{1\theta\theta}}{\partial \theta} + \frac{4}{r}e_{1r\theta} + 2\frac{\partial e_{1r\theta}}{\partial r} = \frac{1}{r}\frac{\partial p_1}{\partial \theta}, \tag{3.14b}$$

$$e_{1rr} + e_{1\theta\theta} = 0, \tag{3.14c}$$

with the boundary conditions,

$$\left.\begin{aligned} u_1 &= 0 \\ \frac{\partial u_1}{\partial r} &= 0 \end{aligned}\right\} \quad \text{at } r = 1, \tag{3.15a}$$

$$\left.\begin{aligned} e_{1r\theta} &= \frac{2}{R_0^3}\frac{\partial R_1}{\partial \theta} \\ p_1 &= 2e_{1rr} + \frac{4}{R_0^3}R_1 \end{aligned}\right\} \quad \text{at } r = R_0. \tag{3.15b}$$

These last two boundary conditions can be rearranged using (3.6) and (3.14b,c) to give

$$\left.\begin{aligned} R_0^2 u_1'' + R_0 u_1' + (k^2-1)u_1 &= \frac{4k^2}{R_0^2} R_1 \\ R_0^3 u_1''' + 2R_0^2 u_1'' - (1+3k^2) R_0 u_1' + (1-k^2)u_1 &= -\frac{4k^2}{R_0^2} R_1 \end{aligned}\right\} \quad \text{at } r = R_0, \quad (3.15c)$$

while (3.11) implies that

$$u_1 = \left(\mathcal{G} + \frac{1}{R_0^2}\right) R_1 \quad \text{at } r = R_0. \quad (3.15d)$$

Equations (3.14) can be combined into a 4th–order ordinary differential equation for u_1

$$\frac{1}{2k^2} r^4 u_1'''' + \frac{3}{k^2} r^3 u_1''' + \left(\frac{5}{2k^2} - 1\right) r^2 u_1'' - \left(1 + \frac{1}{2k^2}\right) r u_1' + \left(\frac{k^2}{2} + \frac{1}{2k^2} - 1\right) u_1 = 0, \quad (3.16)$$

where prime denotes derivative with respect to r, which has the general solution

$$u_1 = c_1 r^{1+k} + c_2 r^{1-k} + c_3 r^{-1+k} + c_4 r^{-1-k}. \quad (3.17)$$

This general solution can be used in (3.15a,c,d) to give homogeneous equations for c_1, c_2, c_3, c_4 and R_1 (Appendix A). The solvability condition gives the dispersion relation

$$\begin{vmatrix} 1 & 1 & 1 & 1 & 0 \\ 1+k & 1-k & k-1 & -(k+1) & 0 \\ (1+k)R_0^{1+k} & (k-1)R_0^{1-k} & (k-1)R_0^{k-1} & (1+k)R_0^{-(1+k)} & -\dfrac{2k}{R_0^2} \\ k(1+k)R_0^{1+k} & k(1-k)R_0^{1-k} & (k^2+k-2)R_0^{k-1} & (2-k^2+k)R_0^{-(1+k)} & -\dfrac{2k}{R_0^2} \\ R_0^{1+k} & R_0^{1-k} & R_0^{k-1} & R_0^{-(1+k)} & -\mathcal{G} - \dfrac{1}{R_0^2} \end{vmatrix} = 0, \quad (3.18)$$

which can be evaluated to yield the growthrate

$$\mathcal{G} = -\frac{1}{R_0^2} + \frac{2k^2 \left(R_0^2 - 1\right)^2}{k^2 R_0^2 \left(R_0^2 - 1\right)^2 + R_0^4 \left(R_0^k + R_0^{-k}\right)^2}, \quad (3.19)$$

which is found to be consistent with the numerical solution of the full model that we described in the previous section (Fig. 7).

In the limit $R_0 \to 1$ the growthrate approaches -1 for all modes and the front is stable. This limit is equivalent to the limit $r_G \to \infty$ so that $\delta \to 0$, which implies that a planer interface is stable. The growthrate becomes less negative as R_0 increases, and in the limit $R_0 \to \infty$, for any finite k we evaluate

$$\mathcal{G}(k) \sim \frac{1}{R_0^2} \left(-1 + \frac{2k^2}{k^2 + R_0^{2k-2}}\right), \quad (3.20)$$

which implies that $\mathcal{G} \leqslant 0$ for all k in the Newtonian limit, and confirms the results of the stability analysis for power–law fluid that the neutral curve doesn't intersect $n = 1$ (Fig. 5). An important feature of the Newtonian–fluid growthrate is that in the range $R_0 < 2 \Leftrightarrow \delta < 1$, the growthrate has a local maximum at approximately $R_0 - 1 = \delta \sim 1/k$ (Fig. 7). This thickness–wavenumber relation coincides with the relation that the most–unstable modes satisfy in the case of strain–rate–softening fluid ($n > 1$), as indicated

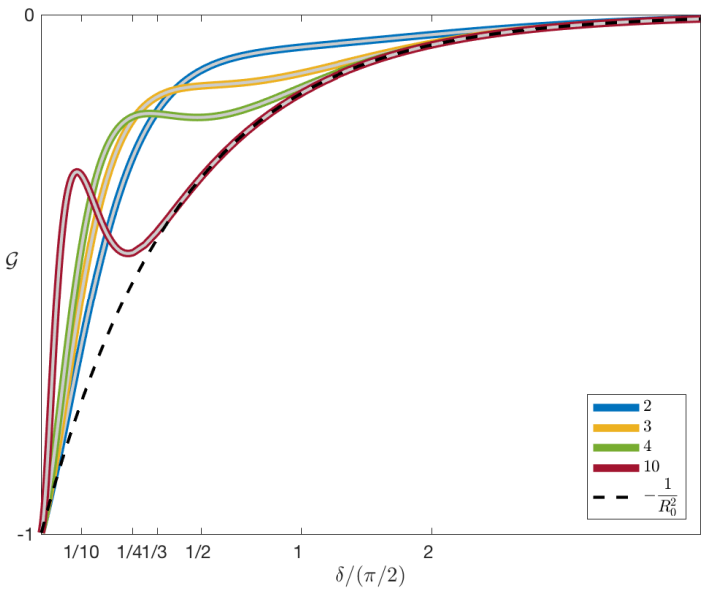

FIGURE 7. The growthrate for $n = 1$ as a function of the width of the fluid layer normalised by $\pi/2$ for $k = 2, 3, 4, 10$, evaluated by the asymptotic solution eq. (3.19) (color), and validated numerically by the full–model solution (▬). The base–state rate–of–strain contribution to the growthrate $-1/R_0^2$ is marked by (- -).

in Fig. 4, suggesting that these local maxima in the $n = 1$ case develop into the global maxima at higher n. This implies that the destabilising mechanism is present in the Newtonian limit. In particular, (3.19) implies that $u_1(R_0)$ is positive, with a maximum, and it is only the geometrical stretching $-1/R_0^2$ that keeps the flow stable. We elaborate on this point when discussing the instability mechanism in §4.

3.5. *Asymptotic solutions: The thin–film approximation*

To get deeper insights into the instability mechanism, we take advantage of the fact that at early time the width of the annular sheet of fluid $r_N(t) - r_G$ is small compared with r_G so that a thin–film theory could be utilised to describe the leading–order flow. In this limit the radius is $r = 1 + \delta\xi$, where $\delta \ll 1$ and ξ is the dimensionless coordinate of order 1, implying that $dr = \delta d\xi$. In addition, we let U, V and P denote the magnitude of the perturbation fields corresponding to u_1, v_1 and p_1, respectively. Next we expand the full perturbation equations for the momentum and mass balance (3.10)

$$\frac{1}{n}\frac{\partial}{\partial r}\left(2\mu_0\frac{\partial u_1}{\partial r}\right) + \frac{4\mu_0}{rn}\frac{\partial u_1}{\partial r} + \frac{1}{r}\frac{\partial}{\partial\theta}\left[\mu_0\left(\frac{1}{r}\frac{\partial u_1}{\partial\theta} + \frac{\partial v_1}{\partial r} - \frac{v_1}{r}\right)\right] = \frac{\partial p_1}{\partial r}, \tag{3.21a}$$

$$\frac{1}{rn}\frac{\partial}{\partial\theta}\left[\frac{2\mu_0}{r}\left(\frac{\partial v_1}{\partial\theta} + u_1\right)\right] + \frac{2\mu_0}{r}\left(\frac{1}{r}\frac{\partial u_1}{\partial\theta} + \frac{\partial v_1}{\partial r} - \frac{v_1}{r}\right) + \frac{\partial}{\partial r}\left[\mu_0\left(\frac{1}{r}\frac{\partial u_1}{\partial\theta} + \frac{\partial v_1}{\partial r} - \frac{v_1}{r}\right)\right] = \frac{1}{r}\frac{\partial p_1}{\partial\theta}, \tag{3.21b}$$

$$\frac{\partial u_1}{\partial r} + \frac{1}{r}\frac{\partial v_1}{\partial\theta} + \frac{u_1}{r} = 0, \tag{3.21c}$$

§3.4	All δ	All k	–	$n = 1$
§3.5.1	$\delta \ll 1$	$k \gg 1$	$\delta k \approx 1$	All n
§3.5.2	$\delta \ll 1$	$k \gg 1$	$\delta k \approx 1$	$n \gg 1$
§3.5.3	$\delta \ll 1$	$k \gg 1$	$\delta k \approx 1$	$n \ll 1$

TABLE 1. Asymptotic solutions and distinguished limits considered.

and represent them in terms of the thin–layer coordinate and the dimensionless perturbation fields (tildes) $u_1 = U\tilde{u}_1, v_1 = V\tilde{v}_1$ and $p_1 = P\tilde{p}_1$ to get

$$\frac{2U}{n\delta^2}\frac{\partial}{\partial\xi}\left(\mu_0\frac{\partial\tilde{u}_1}{\partial\xi}\right) + \frac{4\mu_0}{(1+\delta\xi)n}\frac{U}{\delta}\frac{\partial\tilde{u}_1}{\partial\xi} + \frac{\mu_0}{1+\delta\xi}\frac{\partial}{\partial\theta}\left(\frac{U}{1+\delta\xi}\frac{\partial\tilde{u}_1}{\partial\theta} + \frac{V}{\delta}\frac{\partial\tilde{v}_1}{\partial\xi} - \frac{V\tilde{v}_1}{1+\delta\xi}\right) = \frac{P}{\delta}\frac{\partial\tilde{p}_1}{\partial\xi}, \tag{3.22a}$$

$$\frac{2\mu_0}{(1+\delta\xi)^2 n}\left(V\frac{\partial^2\tilde{v}_1}{\partial\theta^2} + U\frac{\partial\tilde{u}_1}{\partial\theta}\right) + \frac{2\mu_0}{1+\delta\xi}\left(\frac{U}{1+\delta\xi}\frac{\partial\tilde{u}_1}{\partial\theta} + \frac{V}{\delta}\frac{\partial\tilde{v}_1}{\partial\xi} - \frac{V\tilde{v}_1}{1+\delta\xi}\right) + \frac{1}{\delta}\frac{\partial}{\partial\xi}\left[\mu_0\left(\frac{U}{1+\delta\xi}\frac{\partial\tilde{u}_1}{\partial\theta} + \frac{V}{\delta}\frac{\partial\tilde{v}_1}{\partial\xi} - \frac{V\tilde{v}_1}{1+\delta\xi}\right)\right] = \frac{P}{1+\delta\xi}\frac{\partial\tilde{p}_1}{\partial\theta}, \tag{3.22b}$$

$$\frac{U}{\delta}\frac{\partial\tilde{u}_1}{\partial\xi} + \frac{V}{1+\delta\xi}\frac{\partial\tilde{v}_1}{\partial\theta} + \frac{U\tilde{u}_1}{1+\delta\xi} = 0, \tag{3.22c}$$

where $\mu_0 = (1+\delta\xi)^{2\left(1-\frac{1}{n}\right)}$. The corresponding boundary conditions are

$$\tilde{u}_1 = \frac{\partial\tilde{u}_1}{\partial\xi} = 0 \qquad \text{at } \xi = 0, \tag{3.23a}$$

$$\left.\begin{aligned} \frac{1}{2}\left(\frac{ikU}{1+\delta}\tilde{u}_1 + \frac{V}{\delta}\frac{\partial\tilde{v}_1}{\partial\xi} - \frac{V\tilde{v}_1}{1+\delta}\right) &= \frac{2ik}{(1+\delta)^3}R_1 \\ 2U(1+\delta)^{2\left(1-\frac{1}{n}\right)}\frac{1}{n\delta}\frac{\partial\tilde{u}_1}{\partial\xi} + 4(1+\delta)^{2\left(1-\frac{1}{n}\right)-3}R_1 &= P\tilde{p}_1 \end{aligned}\right\} \quad \text{at } \xi = 1. \tag{3.23b}$$

Since n can be any positive number and k can be any positive integer, we now consider several distinguished limits of this thin–film model as shown in Table 1.

3.5.1. *The distinguished limit $\delta \ll 1$, $k \gg 1$, $\delta k \approx 1$*

We consider the distinguished limit in which $\delta \ll 1$, $k \gg 1$ while $\delta k \approx 1$. The dominant balance in (3.22c) implies that $U \sim V$, and (3.22a) implies that $Pk \sim V/\delta^2$. Therefore to leading–order the conservation equations simplify to (tildes removed)

$$\frac{2u_1''}{n\delta^2} - k^2 u_1 + \frac{ik}{\delta}v_1' = \frac{p_1'}{\delta}, \tag{3.24a}$$

$$-\frac{2k^2}{n}v_1 + \frac{ik}{\delta}u_1' + \frac{1}{\delta^2}v_1'' = ikp_1, \tag{3.24b}$$

$$\frac{1}{\delta}u_1' + ikv_1 = 0, \tag{3.24c}$$

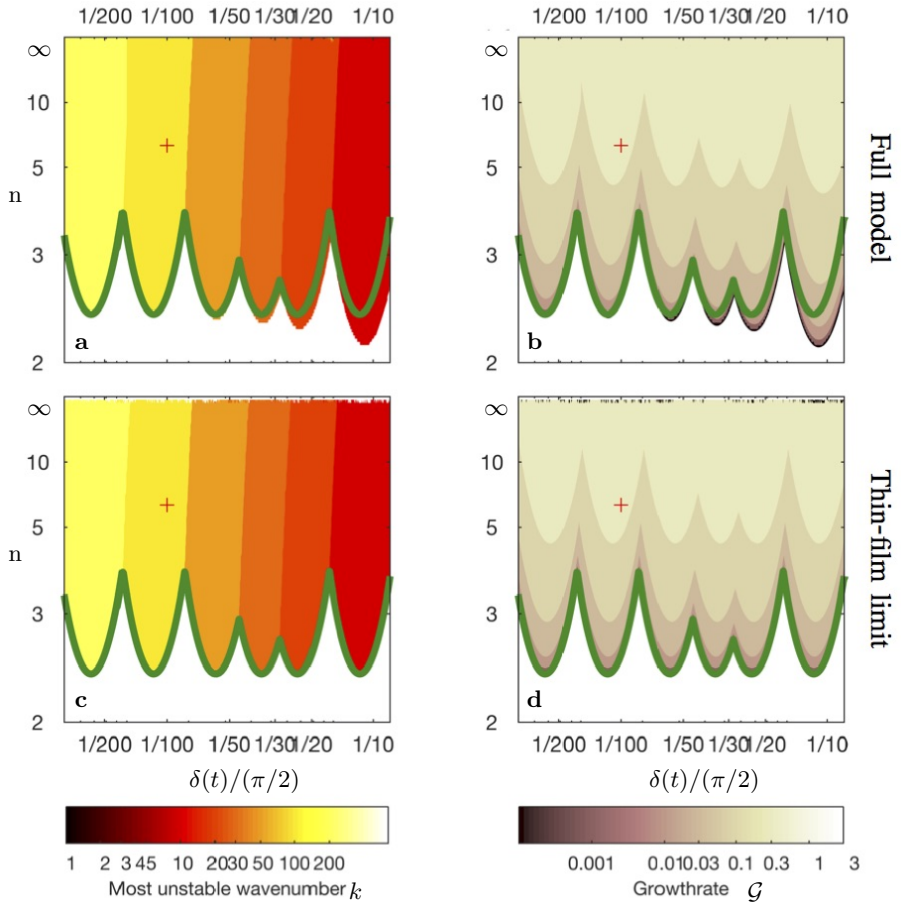

FIGURE 8. Comparison of the predicted unstable modes between the full perturbation model (a,b) and the thin–film model (c,d), showing the most–unstable wavenumbers (left column) and the corresponding growthrate (right column) as a function of n and the annulus width $\delta/(\pi/2)$, among $k = 10, 20, 30, 50, 100, 200$. In all panels, ▬ mark the global neutral curve ($\mathcal{G} = 0$) predicted by the thin–film model for that specific set of wavenumbers. The details of the secondary flow for $n = 6$ and $\delta = (\pi/2)/100$ (+) is shown in Fig. 9.

where primes denote derivatives with respect to the thin–film coordinate ξ, the leading–order boundary conditions are

$$u_1(0) = 0, \quad v_1(0) = 0, \quad ik\delta u_1(1) + v_1'(1) = 4i\delta k R_1, \quad p_1(1) = \frac{2}{n\delta} u_1'(1), \qquad (3.24d)$$

and the corresponding growthrate is

$$\mathcal{G} = -1 + u_1(\xi = 1). \qquad (3.25)$$

To solve for u_1 we combine equations (3.24a-c) to get the following 4th–order differential equation for $u_1(\xi)$

$$u_1^{iv} - \frac{2(2-n)}{n} K^2 u_1'' + K^4 u_1 = 0, \qquad (3.26)$$

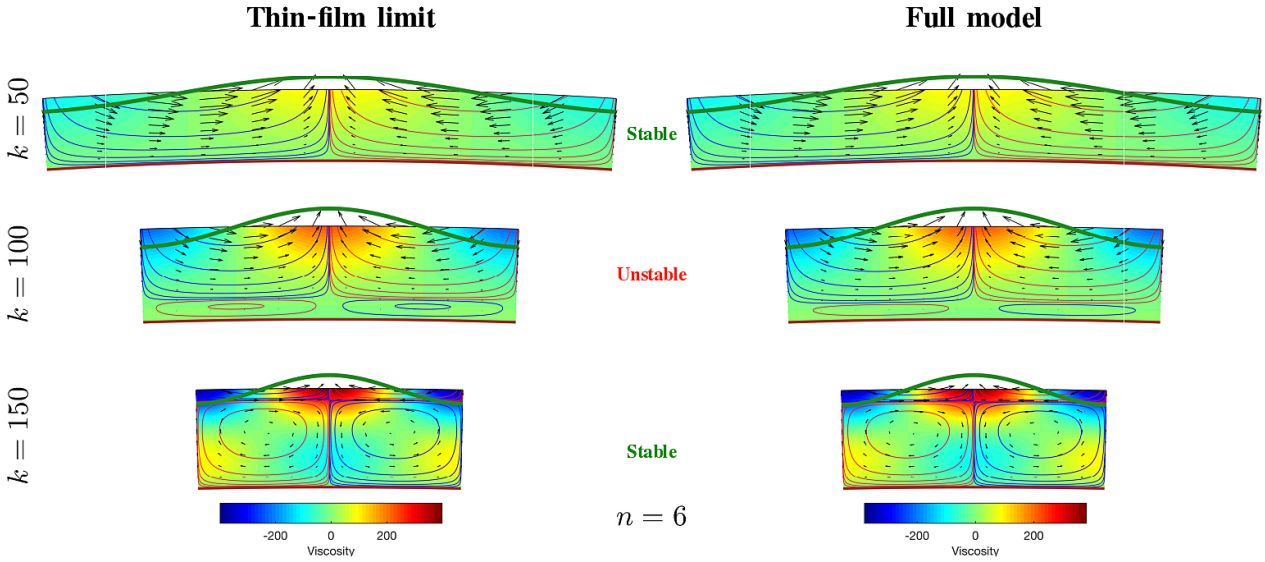

FIGURE 9. One–wavelength sections of the two–dimensional flow for $\delta/(\pi/2) = 1/100$ and $n = 6$, comparing the perturbation flow (arrows and streamlines) and viscosity (color) obtained by the thin–film approximation (left column) and by the full solution (right column), for the wavenumbers $k = 50, 100, 150$. The perturbed front is marked with ▬. The value of δ and n correspond to the + in Fig. 8. The specific growthrates are (from low to high wavenumbers) $\mathcal{G} \approx -0.14, +0.40, -0.32$ (Thin film) and $\mathcal{G} \approx -0.12, +0.42, -0.27$ (full model). Streamlines absolute value: 0.0005, 0.002, 0.008, 0.032, 0.128, 0.512.

where $K \equiv k\delta$. We substitute in the solution the first two boundary conditions in (3.24*d*) to get

$$u_1 = A \sinh aK\xi \sin bK\xi + B\left(\sinh aK\xi \cos bK\xi - \frac{a}{b}\cosh aK\xi \sin bK\xi\right), \tag{3.27}$$

where a and b satisfy the relations

$$a^2 - b^2 = \frac{2-n}{n}, \quad ab = \frac{\sqrt{n-1}}{n}. \tag{3.28}$$

All four solutions for a and b result in the same $u_1(\xi)$. Choosing for example $a = 1/\sqrt{n}$ and $b = \sqrt{(n-1)/n}$ and using the other two boundary conditions in (3.24*d*) to solve for the growthrate, we find that

$$\mathcal{G} = -1 + \frac{2n \sin^2\left(K\sqrt{\frac{n-1}{n}}\right)}{\sin^2\left(K\sqrt{\frac{n-1}{n}}\right) + (n-1)\cosh^2\left(\frac{K}{\sqrt{n}}\right)}. \tag{3.29}$$

This prediction of the growthrate and of the most–unstable wavenumber is consistent with the solution of the full equations (3.10) in the thin–film limit (Fig. 8). Instability emerges in the thin–film limit for $n \gtrsim 2.5$. The neutral curve of the full solution follows the same path, but a departure with the thin–film approximation grows with δ and is noticable near $\delta/(\pi/2) \sim 1/20$ in Fig. 8, and by the time $\delta/(\pi/2) \sim 1/5$, that neutral curve intersects $n = 2$ (Fig. 5). Nevertheless, the prediction of the most unstable wavenumber for $n \gtrsim 2.5$ is still consistent between the two models even for larger δ. A more detailed comparison of the secondary flow between the full and the thin–film models indicates that the two models are highly consistent (Fig. 9). In the Newtonian limit ($n \to 1$) the

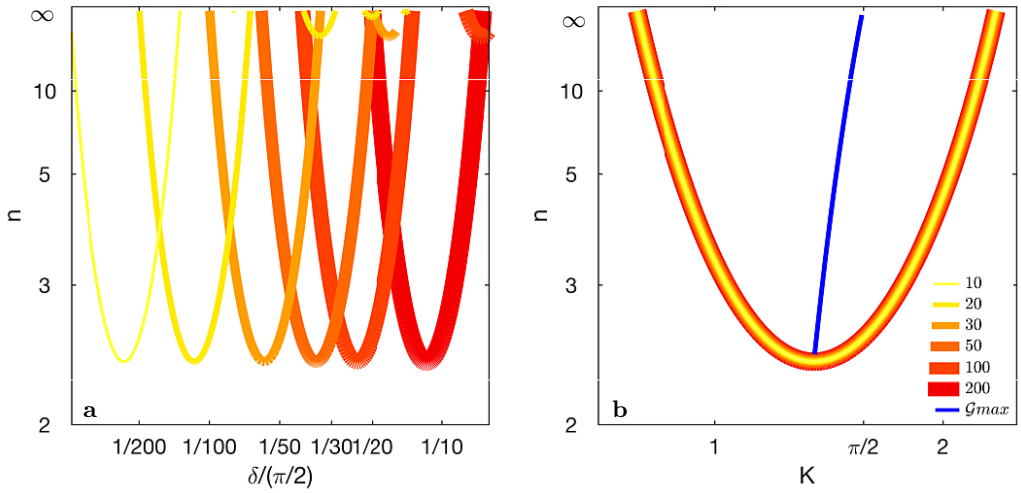

FIGURE 10. (**a**) Neutral curves (color) predicted by the thin–film approximation for a set of wavenumbers $k = 10, 20, 30, 50, 100, 200$ as a function of the power–law exponent n and of the normalised thickness of the annular layer of fluid $\delta/(\pi/2)$. The unstable region is always above the neutral cures. (**b**) The same neutral curves as in panel (a), but as a function of the dimensionless wavenumber $K \equiv k\delta$ collapse into a universal curve. The value of K that corresponds to the maximum growthrate for each n is marked with (▬).

growthrate is

$$\mathcal{G}_{n\to 1} = -\frac{1 - 2K^2 + \cosh(2K)}{1 + 2K^2 + \cosh(2K)} = -1 + \frac{2K^2}{K^2 + \cosh^2 K}, \tag{3.30a}$$

which is consistent with the growthrate that was obtained in section §3.4 without assuming the thin–film limit, when the same distinguished limit is applied to (3.19). This expression shows more clearly that the growthrate in the Newtonian limit is negative for all K, reconfirming that the Newtonian case is stable.

The consistency with the full model that we demonstrate indicates that the thin–film model preserves the important physical components of the instability mechanism in a framework that is simple enough to present the solution in a closed form. Moreover, the thin–film model consists of only two parameters, n and K, as implied from equation (3.29), rather than the three parameters n, k, δ in the full perturbation model. One consequence of this simplicity is the collapse of the neutral curves for individual wavenumbers (Fig. 10a) into a single universal curve (Fig. 10b). This result was anticipated based on the analysis of the full model, as indicated in Fig. 4b. The existence of a universal neutral curve also implies a universal maximum–growthrate curve, based on (3.29), that marks the most unstable wavenumbers K as a function of n (Fig. 10b). This result suggests that $K \sim \pi/2$ is a good approximation for the most–unstable wavenumber, particularly at large values of n. In the next section we investigate an even simpler version of the thin–film model, focusing on the $n \gg 1$ limit.

3.5.2. *The distinguished limit* $\delta \ll 1,\ k \gg 1, \delta k \approx 1, n \gg 1$

Consider now the distinguished limit $\delta \ll 1$, $k \gg 1$, $\delta k \approx 1$ and $n \gg 1$, which represents the perfectly plastic limit or a fluid that is ultra strain–rate softening, such as paste or Plasticine. Although the growthrate in this case can be derived directly by considering

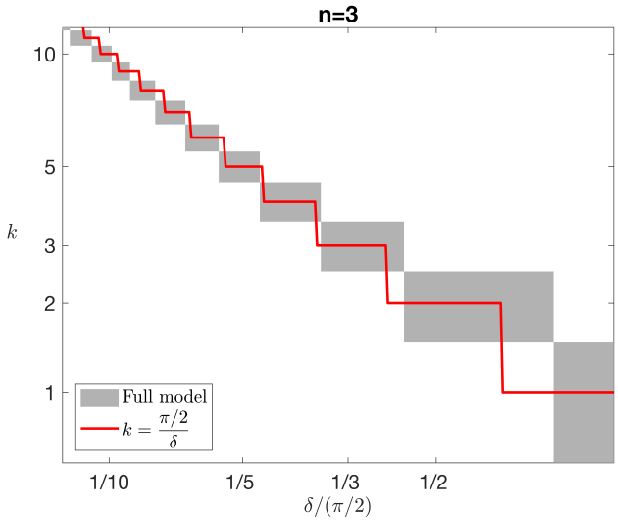

FIGURE 11. The instantaneous most–unstable wavenumber for $n = 3$ as a function of the thickness of the fluid annulus δ, evaluated by the full–model solution (▬), and by the thin–film and $n \gg 1$ limit (▬) according to the round value of the wavenumber predicted by eq. (3.35).

the limit $n \to \infty$ in (3.29), we choose to present the explicit model equations, as they become useful in analysing the physical mechanism in §4. The dominant balance can be derived directly from equations (3.24) by taking the limit $n \to \infty$, which leads to a thin–film model that is independent of n

$$-k^2 u_1 + \frac{ik}{\delta} v_1' = \frac{p_1'}{\delta}, \tag{3.31a}$$

$$\frac{ik}{\delta} u_1' + \frac{1}{\delta^2} v_1'' = ikp_1, \tag{3.31b}$$

$$\frac{1}{\delta} u_1' + ikv_1 = 0, \tag{3.31c}$$

with the boundary conditions

$$u_1(0) = 0, \quad v_1(0) = 0, \quad ik\delta u_1(1) + v_1'(1) = 4i\delta k, \quad p_1(1) = 0. \tag{3.31d}$$

As before, equations (3.31a-c) can be combined into a single ODE

$$u_1^{iv} + 2K^2 u_1'' + K^4 u_1 = 0, \tag{3.32}$$

and the growthrate in this distinguished limit is

$$\mathcal{G}_{n\to\infty} = -\cos(2K) \tag{3.33}$$

to leading order. This implies that the unstable wavenumbers are in the range

$$\frac{1}{4}\frac{\pi}{\delta} \leqslant k_{n\to\infty} \leqslant \frac{3}{4}\frac{\pi}{\delta}, \tag{3.34}$$

and that the maximum growthrate occurs for $2K = \pi$, which corresponds to a most unstable wavenumber k given by

$$k \equiv \frac{\pi/2}{\delta} = \frac{\pi/2}{R_0 - 1}. \tag{3.35}$$

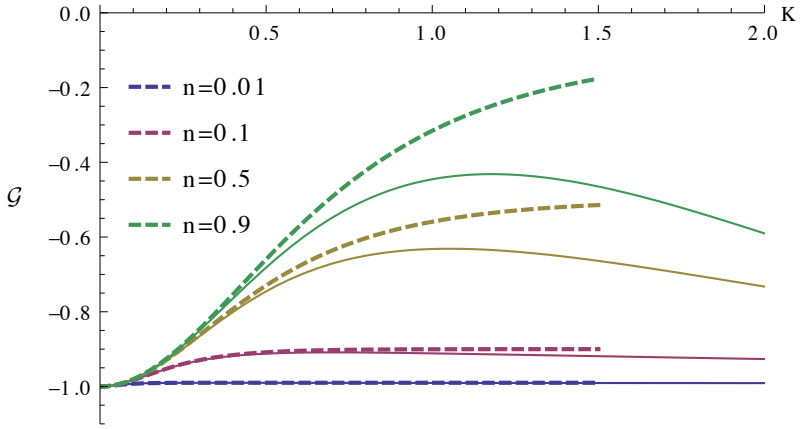

FIGURE 12. The growthrate at the thin–film approximation and the limit $n \ll 1$ (- - -) compared with the complete thin–film solution (——), for n ranging between 1/100 and 9/10.

This distinguished limit turns out to be quite useful in predicting the most–unstable wavenumber also for finite n, as implied from the thin–film solution for finite n (Fig. 10b). Moreover, (3.35) provides a reasonable prediction for the most–unstable wavenumber even for large δ, as implied from a comparison with the solution to the full perturbation model at low value of n (Fig. 11).

There is a special feature of the perfect plastic limit given by eq. (3.33), which is that an infinite sequence of harmonics $K = (j+1/2)\pi$, $j \in Z$ share the maximum growthrate. This allows for the growth of linear, non–sinusoidal disturbances albeit of an identifiable fundamental wavelength.

3.5.3. *The distinguished limit* $\delta \ll 1,\ k \gg 1, \delta k \approx 1, n \ll 1$

Still in the distinguished limit in which $\delta \ll 1$, $k \gg 1$ while $\delta k \approx 1$, we now consider the case $n \ll 1$ where the fluid is ultra strain–rate thickening. In this limit we can use equations (3.24) to find that the leading–order terms are

$$\frac{2u_1''}{n\delta^2} - k^2 u_1 = \frac{p_1'}{\delta}, \tag{3.36a}$$

$$-\frac{2k^2}{n} v_1 + \frac{v_1''}{\delta^2} = ikp_1, \tag{3.36b}$$

$$\frac{1}{\delta} u_1' + ikv_1 = 0, \tag{3.36c}$$

and that the boundary conditions are identical to (3.24*d*). As before, equations (3.36) can be combined into a single ODE

$$u_1^{iv} - \frac{4}{n} K^2 u_1'' + K^4 u_1 = 0, \tag{3.37}$$

and we find that the growthrate in this distinguished limit is

$$\mathcal{G}_{n\to 0} = -1 + n\left(1 - \frac{1}{\cosh(\frac{2K}{\sqrt{n}})}\right) \tag{3.38}$$

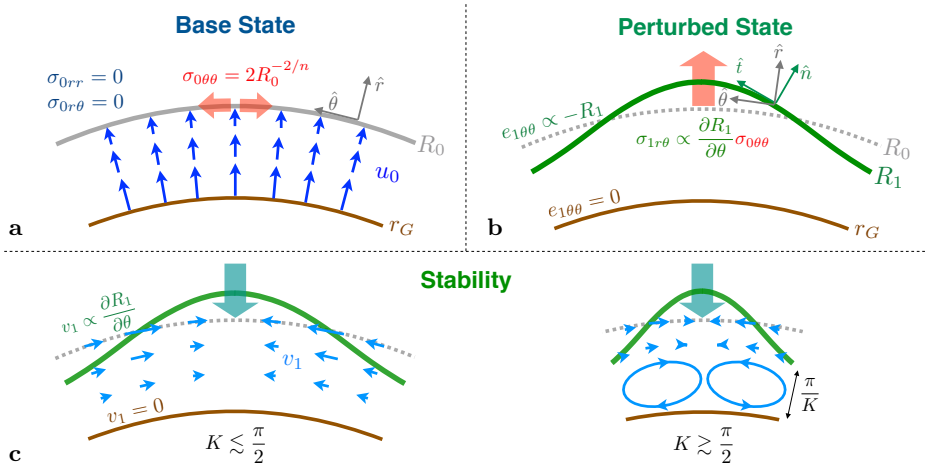

FIGURE 13. (a) The leading front of the base state (▬) is under tension due to non–zero normal stress in the $\hat{\theta}\hat{\theta}$ direction, while the other stress components are zero. (b) The base–state normal stress contributes to tangential stress at the perturbed interface (▬). Therefore, the condition of zero tangential stress at the perturbed front implies a perturbation shear stress at the $\hat{r}\hat{\theta}$ direction of the base front that is proportional to the slope of the perturbed front. (c) The secondary flow following a geometric perturbation (↓) consists of two distinct patterns through which momentum dissipates and stabilises the perturbation: At $K \lesssim \pi/2$, the streamlines stretch circumferentially from frontal depressions to frontal bulges through a relatively long path along which energy is dissipated. At $K \gtrsim \pi/2$, vortices form near the inner boundary and screen the interior from the front, so that less fluid is available to sustain the growth of tongues. The volume covered with vortices grows with K.

to leading order in n, which is negative for all K (e.g., Fig. 12) and is consistent with (3.29) in the limit $n \to 0$.

4. Physical interpretation of the tearing mechanism

4.1. *The structure of the growthrate*

To reveal the physical mechanism behind the instability we now investigate the structure of the growthrate (3.11) by deriving a more explicit expression for the radial perturbation velocity at the front, $u_1(R_0)$. Combining the boundary condition of no–tangential and no–normal stresses (3.12*b*), the perturbation shear stress at the base–state front is

$$\sigma_{1r\theta}(R_0) = \frac{1}{R_0}\frac{\partial R_1}{\partial\theta}\sigma_{0\theta\theta}(R_0). \tag{4.1}$$

By taking a derivative with respect to θ

$$\frac{\partial\sigma_{1r\theta}}{\partial\theta}(R_0) = \frac{1}{R_0}\frac{\partial^2 R_1}{\partial\theta^2}\sigma_{0\theta\theta}(R_0) \tag{4.2}$$

we see that the left hand side is a radial force. Substituting the definition of the shear stress in terms of the perturbation velocities (3.6*c*) leads to

$$\mu_0\frac{\partial}{\partial\theta}\left[\frac{1}{r}\frac{\partial u_1}{\partial\theta} + r\frac{\partial}{\partial r}\left(\frac{v_1}{r}\right)\right] = \frac{1}{R_0}\frac{\partial^2 R_1}{\partial\theta^2}\sigma_{0\theta\theta}, \tag{4.3}$$

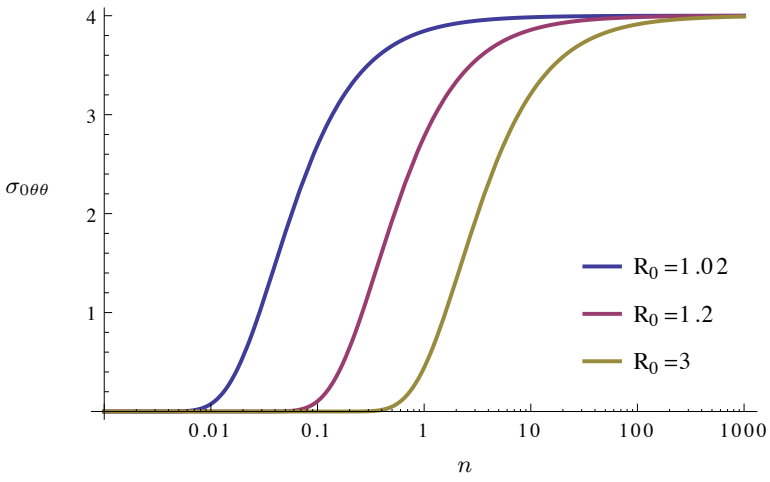

FIGURE 14. The base–flow tension at the leading front is represented by the hoop stress as a function of the fluid exponent.

and solving for u_1 we find that

$$u_1 = \frac{\sigma_{0\theta\theta}}{\mu_0} R_1 + \frac{R_0^2}{k^2} \frac{\partial}{\partial r} \left(\frac{1}{r} \frac{\partial v_1}{\partial \theta} \right). \tag{4.4}$$

Substituting this in the growthrate (3.11) results in

$$\mathcal{G}(k, n, R_0) = -\frac{1}{R_0^2} + \frac{\sigma_{0\theta\theta}}{\mu_0} + \frac{R_0^2}{k^2 R_1} \frac{\partial}{\partial r} \left(\frac{1}{r} \frac{\partial v_1}{\partial \theta} \right), \tag{4.5a}$$

where the three contributions to $\mathcal{G}$ represent the geometric stretching, hoop stress and momentum dissipation. In the thin–film limit ($\partial/\partial r \gg 1/r$) $R_0 \sim 1$ and the growthrate simplifies to

$$\mathcal{G}(K, n) = -1 + 4 - \frac{u_1''}{K^2 R_1}, \tag{4.5b}$$

where the three contributions correspond to those in (4.5a), and where mass continuity at the same limit was used to present the dissipation contribution in terms of the radial velocity.

4.2. *Geometric stretching*

The circular geometry of the flow combined with mass continuity implies that the extensional strain rates of the base flow are $e_{0rr} = \partial u_0/\partial r = -1/R_0^2$ and $e_{0\theta\theta} = u_0/r = 1/R_0^2$. Therefore, as the fluid front advances in circular geometry it stretches azimuthally and slows down radially. This geometrical stretching, which is independent of n and k, gives rise to the first stabilising term in the growthrate (4.5).

4.3. *Instability*

The flow in the base state is axisymmetric and diminishes towards the moving front (Fig. 13a), having radially growing viscosity ($n > 1$), declining viscosity ($n < 1$) or uniform viscosity ($n = 1$). The extensional stress in the $\hat{\theta}\hat{\theta}$ direction (hoop stress) at the base–flow front

$$\sigma_{0\theta\theta}(R_0) = -p_0 + 2\mu_0 e_{0\theta\theta} = 4R_0^{-2/n} \tag{4.6}$$

is always positive (3.4*c*), implying that the fluid front is under tension throughout the evolution. Although the tension grows larger the smaller $R_0 > 1$ is and the more strain–rate softening ($n > 1$) the fluid is (Fig. 14), its contribution to the growthrate (4.5*a*) is the constant $\sigma_{0\theta\theta}/\mu_0 = 4R_0^{-2}$ namely, destabilising and independent of k and n. The instability develops due to the interaction of the base–flow hoop stress with the geometric perturbation: the geometric perturbation of the front forms forward bulges and depressions along the front (Fig. 13b). Consequently, the base–flow hoop stress at the front has a non–zero contribution to the tangential stress along the perturbed interface. Since the total tangential stress along the front must be zero, the perturbation field has a non–zero shear stress along the base–state interface that balances the hoop–stress–geometry contribution (4.1). That is, the interfacial curvature leads to a base–flow hoop stress that leads to a perturbation shear stress due to the perturbed interface. The perturbation shear stress, which is proportional to the slope of the perturbed interface $\sigma_{1r\theta}(R_0) \propto \partial R_1/\partial\theta$ (4.1) forces a secondary flow along the base–flow front to converge into forward bulges in the perturbed interface and diverge from interfacial troughs, independently of the fluid exponent n. Consequently, the secondary flow transports fluid from interfacial troughs to bulges, enhancing the perturbation growth. The development of the instability leads to the relaxation of hoop stresses within the growing fingers, so that no additional fingers form at the edges of existing fingers, as experimental evidence indicate (see Sayag & Worster 2019).

We note that with a planar interface in a two–dimensional geometry, hoop stresses, or extensional stresses transverse to the flow are absent. Therefore, the circular geometry is crucial in generating a base–flow hoop stress, which is the source of the instability.

Another way to think of the instability is in terms of forces. In the thin–film base state, the radial extensional force $\partial\sigma_{0rr}/\partial r$ is positive along a radius (3.4*b*), though it is smaller at the leading front than in the interior due to the base–state hoop stress that stretches the fluid azimuthally. Following a perturbation, the contribution to the extensional force $\partial\sigma_{1rr}/\partial r$ is equivalent, in the thin–film limit, to $-\partial\sigma_{1r\theta}/\partial\theta$, which equals at the leading front to $k^2/R_0\sigma_{0\theta\theta}(R_0)R_1$ (4.2). Therefore, the total extensional force at the front grows along a bulge ($R_1 > 0$) and diminishes along a trough ($R_1 < 0$), resulting in a greater radial force along a forward bulge.

4.4. *Stability and the impact of the fluid exponent n*

The contribution of momentum dissipation to the growthrate (4.5*a*) is also stabilising, but unlike the uniform stabilisation of geometric stretching (§4.2), it depends on both the wavenumber and the fluid exponent. In particular, the mechanism of momentum dissipation is qualitatively different between low and high wavenumbers. To see this we use the growthrate in the thin–film limit (4.5*b*), which has the closed–form solution given by (3.29).

4.4.1. *Long–wavelength limit: Lateral flow*

Expanding (3.29) assuming $K \ll 1$ we find that

$$\mathcal{G}_{K\ll 1} \approx -1 + 2K^2 \tag{4.7}$$

to leading order in K, which tends to -1 in the $K \to 0$ limit. This implies that stability in the small wavenumber K limit ($K \ll \pi/2$) is independent of the fluid exponent n to leading order (Fig. 15). Since $K = k\delta$, this limit corresponds to either small wavenumbers k and thus long wavelengths, or to extremely thin–films. Stability in this long–wavelength limit may result from the relatively long circumferential and open streamlines in the secondary flow, along which the total dissipation of momentum is substantial (Fig. 13c).

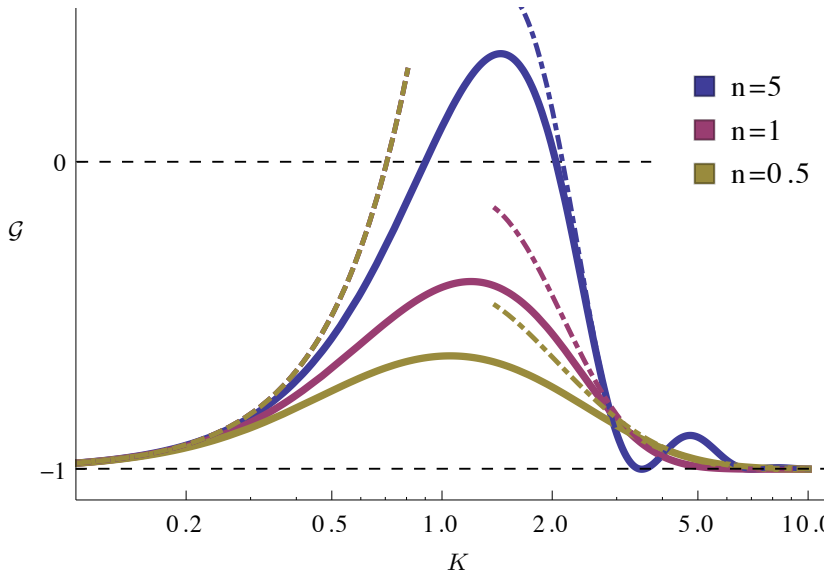

FIGURE 15. The growthrate in the thin–film limit (solid lines) as a function of the effective wavenumber K for fluid exponents $n = 0.5, 1, 5$ (color). The asymptotic behaviour of the growthrate in the small–wavenumber limit ($K \ll 1$) is independent of n to leading order (dash line). In the large wavenumber limit ($K \gg 1$) the growthrate has a leading–order dependence in the fluid exponent (dash–dot).

As the wavelength turns shorter (wavenumber larger) the streamlines get shorter so less momentum dissipates, whereas the destabilising hoop stress remains unchanged, which allows the instability to grow.

4.4.2. *Short–wavelength limit: Vortices*

In the large wavenumber K limit, the growthrate (3.29) has the simplified form

$$\mathcal{G}_{K\gg1} \approx -1 + 2K^2 \left(\frac{\sin(K\sqrt{(n-1)/n})}{K\sqrt{(n-1)/n}\cosh(K/\sqrt{n})} \right)^2, \tag{4.8}$$

which implies that stability in large wavenumbers ($K \gg \pi/2$) depends also on the fluid exponent n to leading order (Fig. 15). This limit corresponds to either large wavenumbers k and thus short wavelengths, or to relatively thicker films. In this short-wavelength limit, we expect dissipation to enhance due to the corresponding large gradients. This is naturally the case for Newtonian fluid due to the constant viscosity. However, for $n \neq 1$ the growth of dissipation with the wavenumber is not straightforward since the strain-rate dependent viscosity also changes. Specifically, the viscosity varies with both the wavenumber and n as implied from eq. (3.8) and Fig. 6. In fact, in the $K \gg 1$ limit the dissipation dominates and is a weak function of n such that $\mathcal{G} \to -1$ in the $K \to \infty$ limit. The sensitivity to n grows at intermediate wavenumbers ($K \approx \pi/2$), in which the dissipation is stronger than the Newtonian case when $n < 1$ and weaker when $n > 1$ (Fig. 15), thereby allowing the instability for strain-rate softening fluids.

Another important consequence of the shortwave limit is the emergence of vortices (closed streamlines) in the secondary flow, which form near the inner boundary and are centered at the boundaries between interfacial depressions and bulges (Fig. 13c). Since the

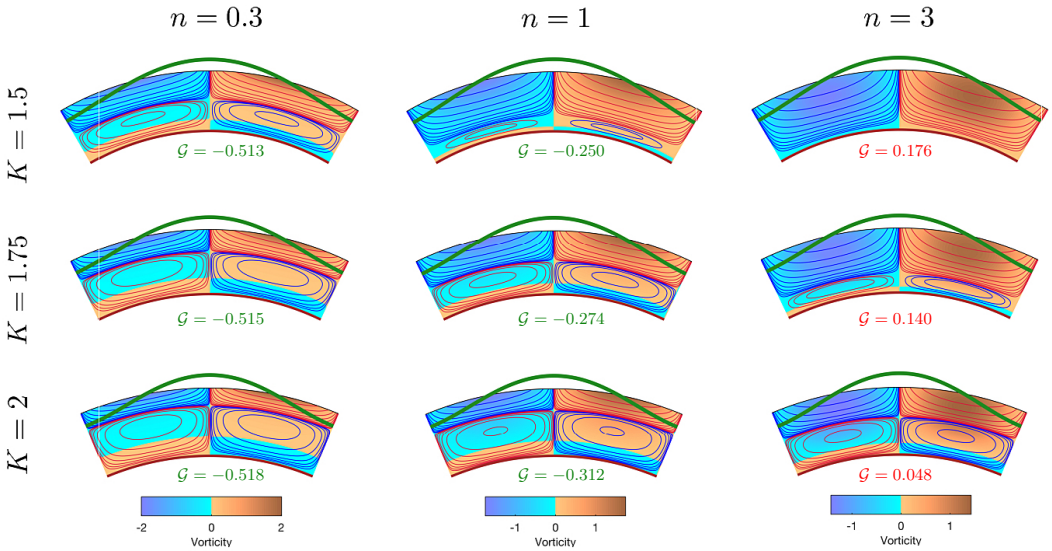

FIGURE 16. The exact perturbation vorticity ω_1/k (color) and streamlines (vortices are clockwise —— or counterclockwise ——) in a one–wavelength sections of the two dimensional flow (▬ marks the perturbed front) for (rows) $K = 1.5, 1.75, 2$ ($\delta = 0.25; k = 6, 7, 8$), and for (columns) $n = 0.3, 1, 3$. The volume covered with vortices grows the larger K is and the smaller n is, and the corresponding growthrate declines. Streamlines absolute value: $0.001, 0.002, 0.004, 0.008, 0.016, 0.032, 0.064, 0.128, 0.256, 0.512$.

mass flux out of a vortex is zero, the fluid that contributes to the growth of perturbation comes from the region without vortices, which gets smaller with K and/or as n declines (Fig. 16). That is, vortices screen the front from the fluid interior, so that there is no secondary–flow mass flux from the vortex region to the front region. Consequently, with the growth of the vortex–covered area with K the radial velocity at the front declines and so is the growthrate.

A measure of the behaviour of the secondary–flow vortices can be provided by the perturbation vorticity

$$\omega_1 \equiv (\boldsymbol{\nabla} \times \boldsymbol{u}_1) \cdot \hat{\boldsymbol{z}} = \frac{\partial v_1}{\partial r} + \frac{v_1}{r} - \frac{1}{r}\frac{\partial u_1}{\partial \theta}, \tag{4.9a}$$

which simplifies in the thin–film limit ($\delta \ll 1$) to

$$\omega_1 \approx \frac{1}{\delta}\frac{\partial v_1}{\partial \xi} - \frac{\partial u_1}{\partial \theta}, \tag{4.9b}$$

to leading order. Considering first the case $n \gg 1$ (§3.5.2), which corresponds to the largest growthrates for all K, the vorticity to leading order in δ

$$\omega_1 = 2\frac{\partial R_1}{\partial \theta}\left[2K\xi \sin(K(1-\xi)) + \cos(K(1+\xi)) + \cos(K(1-\xi))\right] \tag{4.10}$$

has harmonic structure along a radius. Specifically, the signature of ω changes along a radius at a growing frequency with K. This implies that the secondary flow along a radius consists of coexisting clockwise and counterclockwise vortices, whose number grows with K (Fig. 17), or equivalently with both k and δ. This oscillatory structure is slightly reminiscent to flows of strain-rate-softening fluid around a contracting cavity (Dallaston & Hewitt 2014), though with some qualitative differences. Along the boundaries $\xi = 0, 1$,

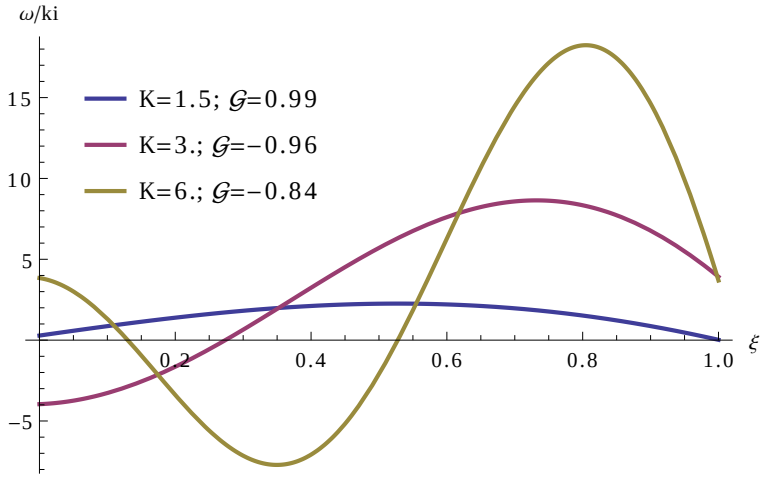

FIGURE 17. The normalised vorticity ω/ki in the limit $n \gg 1$ (4.10) along a radius, for several values of $K = 1.5, 3, 6$.

the perturbation vorticity is

$$\omega_1(1) = 4\frac{\partial R_1}{\partial \theta}\cos^2(K), \tag{4.11a}$$

$$\omega_1(0) = 4\frac{\partial R_1}{\partial \theta}\cos(K), \tag{4.11b}$$

which implies that the vortex rotation at the leading front ($\xi = 1$) follows the sign of the interface slope and is independent of K. However, near the inner boundary ($\xi = 0$) the rotation direction of the vortices changes with both the slope of the leading front and with K. This implies that new vortices emerge at the inner boundary as K grows, and that existing vortices are displaced radially towards the leading front (see video). The azimuthal size of these vortices is half the azimuthal wavelength $\pi\delta/K$, which is equivalent to the radial size (half the radial wavelength), as implied by (4.10). Therefore, the number of vortices along an annulus of thickness δ grows like K/π, forming a vortex street that covers the whole flow domain (Fig. 18b).

When $n \leqslant 1$ (strain–rate thickening), the solution for the radial velocity (3.27) is no longer harmonic because b is imaginary (3.28). Therefore, the vorticity is also non harmonic and the domain of radial size δ can only contain a single vortex (Fig. 18a).

4.5. *Contrast with classical fingering instability*

It is insightful to contrast the present mechanism with the classical viscous–fingering instability. Considering a shear–dominated flow of Newtonian fluid of viscosity μ_d displacing at constant flux Q an ambient Newtonian fluid of viscosity μ_a inside a Hele–Shaw cell of uniform gap h in polar coordinates, the growthrate is (Paterson 1981)

$$\mathcal{G}_{\text{Paterson}} = \frac{Q/h}{2\pi r_0^2}\left[-1 + k\frac{\mu_a - \mu_d}{\mu_a + \mu_d}\right] - \sigma\frac{k(k^2-1)}{r_0^3}\frac{\mu_a\mu_d}{\mu_a + \mu_d}, \tag{4.12a}$$

where $r_0(t)$ is the radius of the base–state interface when the perturbation is applied. Surface tension σ at the fluid–fluid interface is stabilising for all wavenumbers and fluid viscosities. Therefore, for all wavenumbers instability can occur only if the viscosity of the displacing fluid is smaller ($\mu_d < \mu_a$). Particularly, at the absence of surface tension

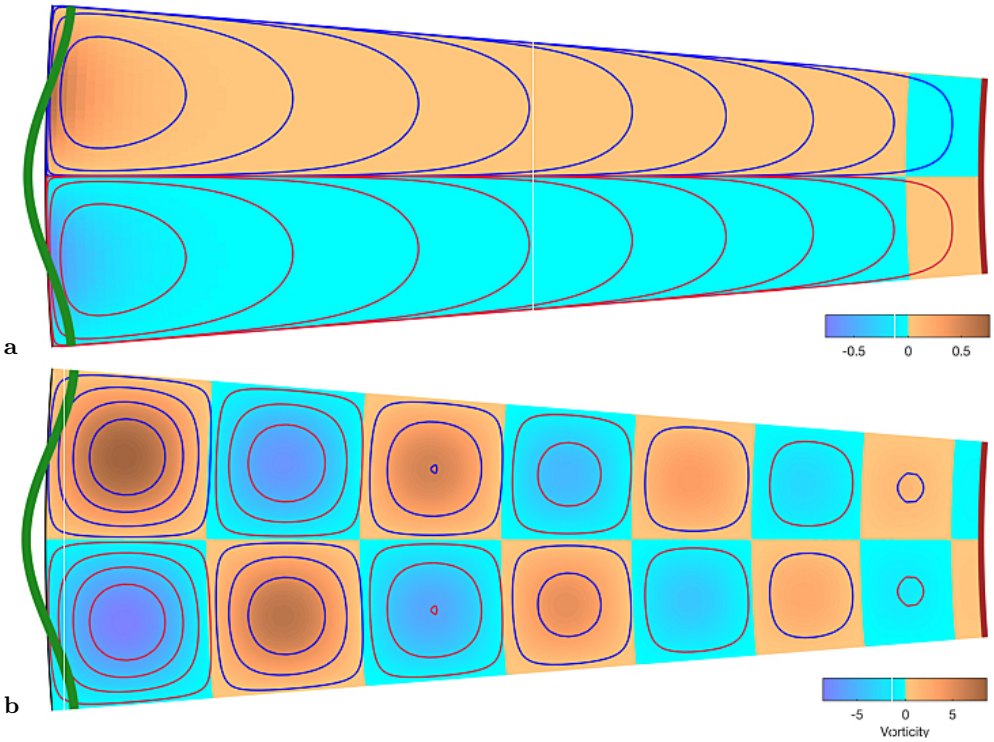

FIGURE 18. Vorticity and vortex street: The exact perturbation vorticity ω_1/k (color) and streamlines (vortices are clockwise — or counterclockwise —) in a one–wavelength sections of the two dimensional flow (▬ marks the perturbed front) for $K = 30$ ($\delta = 0.75; k = 40$) and for (a) $n = 1$ (streamlines absolute value: $0.5, 0.1, 10^{-2}, 10^{-3}, 10^{-4}, 10^{-5}, 10^{-6}, 10^{-7}, 10^{-8}$), and (b) $n = 100$ (streamlines absolute value $0.75, 0.5, 0.25, 0.05$).

and if the viscosity of the displaced fluid is negligible ($\mu_a \ll \mu_d$), as in the flow that we study, the shear–dominated growthrate simplifies to

$$\mathcal{G}_{\text{Paterson}}\Big|_{\sigma=0,\mu_a\ll\mu_d} = \frac{Q/h}{2\pi r_0^2}\left(-1-k\right). \tag{4.12b}$$

In contrast, the flow that we consider in this paper is extensionally dominated and the displacing fluid has a strain–rate dependent viscosity. The resulting dimensional growthrate in the thin–film limit ($\delta \ll 1$)

$$\mathcal{G} = \frac{Q/h}{2\pi r_0^2}\left[-1+\frac{2n\sin^2\left(K\sqrt{\frac{n-1}{n}}\right)}{\sin^2\left(K\sqrt{\frac{n-1}{n}}\right)+(n-1)\cosh^2\left(\frac{K}{\sqrt{n}}\right)}\right] \tag{4.13}$$

implies that if the fluid is strain–rate softening ($n > 1$), the interface is unstable for some wavenumbers $K = k\delta$. Such unstable configuration corresponds to a highly viscous fluid displacing an low–viscosity ambient fluid, a configuration that remains stable in the classical shear–dominated fingering case.

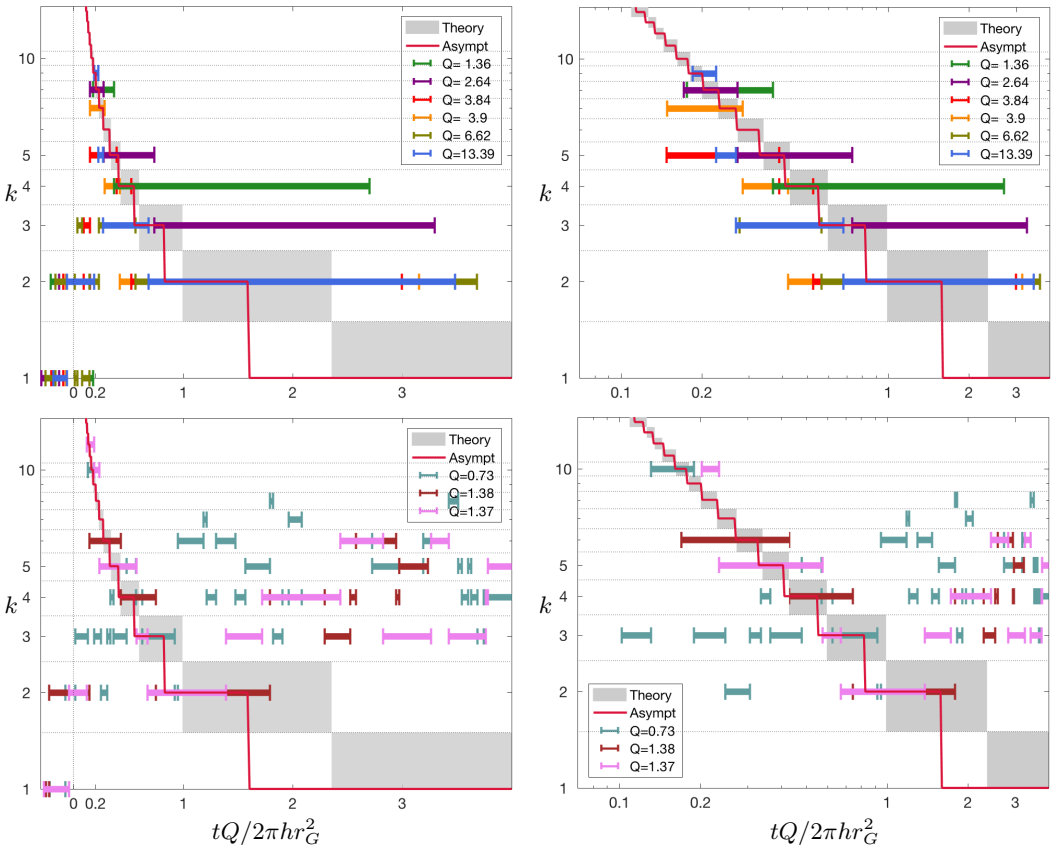

FIGURE 19. Comparison of the predicted most–unstable modes and the time–evolution of the dominant wavenumbers measured in laboratory experiments for $n = 6$ (Sayag & Worster 2019). The experimental measurements (color) represent the dominant Fourier modes that the front is comprised of at each instant for a range of source fluxes $0.7 \lesssim Q \lesssim 13.4$ g/s. Also shown are the corresponding instantaneous most–unstable modes predicted by the full perturbation model (▬), and by the perfectly–plastic ($n \gg 1$) thin–film model (5.1) (▬). (Top row) Experiments that converge to an integer wavenumber. (Bottom row) Experiments whose late–time pattern is stochastic. Results are presented in log–linear scale (left column) and log–log scale (right column), in which the initial transition to high wavenumber is truncated.

5. Consistency with experimental evidence

The theory we have developed thus far is aimed to explain the spatio–temporal patterns that were discovered in a series of laboratory experiments with strain–rate–softening polymer solutions in part I (Sayag & Worster 2019). One important result of these experiments is that the fingered interfaces coarsened over time: As the front of the displacing fluid evolved, the number of floating tongues declined through the progressive closure of some of the tears that separated them, resulting in the merging of adjacent tongues into wider ones. This coarsening or cascade of the dominant wavenumbers, has either converged in time to a lower integer wavenumber, or kept alternating, apparently stochastically, within a range of lower wavenumbers. The results of these experiments were combined into a single graph that shows the evolution of the dominant wavenumbers for the different source flux used (Fig. 9b, Sayag & Worster 2019), in which time

was non dimensionalised with the characteristic scale $\mathcal{T} = 2\pi h r_G^2/Q$ that is also used in the theoretical part (2.6).

The wavenumber–cascade mechanism that we observed experimentally in part I (Sayag & Worster 2019) was operating also when the propagating front was far from the initial circular state, which suggests that it is primarily a nonlinear process. Therefore, there is no apparent reason to expect that the present linear–stability analysis can predict such late–time evolution in the experiments that departs from a circular base state by far. And yet, our theoretical results in the present part also involve a wavenumber cascade. Specifically, for a fixed n in the full linear theory the most–unstable wavenumber declines monotonically with δ. This implies that an unstable front will develop more fingers the earlier the perturbation is made, while fewer fingers will emerge following a perturbation at later times (Fig. 5a). Therefore, we evaluate the instantaneous most–unstable wavenumbers as a function of the base–state thickness δ, as in Fig. 11 but replacing $\delta(t)$ with the explicit dependence on time (3.3), and consider this as a time evolution of the dominant wavenumber. We find that this interpretation of the dependence of the most–unstable wavenumber on the base–state thickness $\delta(t)$ provides a consistent prediction to the initial cascading evolution of the measured dominant wavenumbers (Fig. 19). Furthermore, the prediction of the perfectly–plastic thin–film model for the most–unstable wavenumber (3.35) that is written explicitly in terms of time

$$k_{\max} = \frac{\pi}{2}\left[-1 + \sqrt{\frac{Q}{\pi h r_G^2}t + 1}\right]^{-1} \tag{5.1}$$

also provides a surprisingly consistent prediction for the experimental evolution of the dominant wavenumbers (Fig. 19).

The apparent correspondence between the linear–theory prediction and the cascading phase of the experimental observations is surprising. It implies that at any instant the dominant wavenumber of an experimental pattern, which can be far from a circular shape, is equivalent to the most–unstable wavenumber of a perturbed circular state that has the same volume. This appears to suggest that the wavenumber the system settles on is determined to leading order by the total discharged volume, and that other interactions may be secondary.

Our experimental observations suggest that throughout their evolution there was no apparent flow within the tongues, and that they were displaced as solid objects. The most active flow in the free–slip domain ($r > r_G$) seemed to concentrate within a thin region of width $\approx h$ near r_G. This may imply that the finite–time evolution of the patterns is determined by the flow in the vicinity of r_G and that the tongues are passive components. The interpretation of our theoretical results predicts that the cascade of wavenumbers ends at $k = 1$. Such a situation was not observed experimentally, apart of some experimental indications of a trend toward a $k = 1$ mode at the high–end flux regime (Sayag & Worster 2019).

The transition at low Q to a stochastic late-time evolution, which we identified experimentally (Fig. 19, bottom row) is not captured by the theoretical model. This could be simply a consequence of late time evolution that our linear model cannot resolve. It could also be a result of the relatively simple constitutive model that we used. For example, accounting for a low strain-rate behaviour such as bounded viscosity should introduce another timescale, which may lead to the differentiation between a regular and stochastic evolution with respect to Q. The interaction with the flow of the ambient fluid within the tears may also have an effect, though we do not account for it at present.

6. Conclusions

Inspired by the experimental study in part I (Sayag & Worster 2019), we developed a model to investigate the development of the observed tear–like patterns and their coarsening in time. Our theoretical model includes three elements that we believe are critical to the appearance of the instability: the free–slip conditions along the base and the surface boundaries of the displacing fluid; the circular geometry that imposes circumferential tension along the leading front; and the nonlinear deformation law of the displacing fluid. We found that axisymmetric solutions can become linearly unstable, having a most–unstable wavenumber that is inversely proportional to the thickness of the base state $\delta(t)$, to leading order. Consequently, the thicker the base–flow annular layer is, the smaller the number of tears that would evolve. The mechanism of the instability appears fundamentally different from that of the classical viscous fingering: The source of the instability is the base–flow hoop stress along the leading front. The projection of that stress over the perturbed interfacial geometry results in a perturbation shear stress along the base–flow front that varies azimuthally with the shape of the perturbed front. Such shear–stress distribution results in circumferential flow along the interface that converges into forward bulges and diverges from troughs in the perturbed interface and thus sustains the perturbation growth. We emphasise that the destabilising hoop stress is independent of the wavenumber and of the nonlinearity of the fluid. Rather, the base–flow hoop stress is a consequence of the flow geometry and it is present for all fluid exponents and particularly for both Newtonian or strain–rate–softening fluids. In contrast, the momentum dissipation associated with shear suppresses the perturbations through two different mechanisms at low and high wavenumbers. At the lower–end wavenumbers the secondary flow consists of open circumferential streamlines along which fluid is carried from perturbation depressions to perturbation bulges on a relatively long dissipative path. At the higher–end wavenumbers the dissipation is modified by larger velocity gradients, and the secondary flow consists of vortices that screen perturbation flow from the leading front. The combined impact of these stabilising mechanisms is weakest at wavenumbers $\sim 1/\delta$ and the more strain–rate softening the fluid is. This defines the wavenumbers that grow fastest and that dominate the front pattern.

We find that our fluid–mechanical approach to explain a phenomenon that involves tear–like patterns leads to predictions that are consistent with some major characteristics of the experimental measurements of part I, including the inverse–cascade of the dominant wavenumber, which is predominantly a nonlinear process. Our theoretical model relates to power–law fluids and neglects other potential non–Newtonian properties. The fact that the model includes a single dimensionless number n, associated with the way the fluid viscosity responds to strain rate, implies that the patterns that we observed in polymer solutions may be dynamically similar to other strain–rate–softening fluids under circular extension in inertia–free flow, independently of the spatio–temporal scales of the flow and independently of the material microscopic structures. Particularly, our results may apply to systems ranging from pastes squeezed in laboratory scale to polycrystalline ice creeping into the open ocean on a global scale.

Acknowledgements: RS thanks SIDEER and BIDR in Ben-Gurion University, Israel, for financial support, and to DAMTP, University of Cambridge, UK, where some of this research had took place. This research was supported by the Israel Science Foundation (grant No. 1368/16).

Appendix A. The Newtonian-fluid limit $n = 1$

The coefficients $c_{1\ldots4}$ of the Newtonian-limit solution (3.17) are

$$
\begin{aligned}
c_1 &= \frac{k\left(R_0^{2k} + k\left(R_0^2 - 1\right) + 1\right)}{k^2 R_0^{k+1} - 2\left(k^2 - 1\right) R_0^{k+3} + k^2 R_0^{k+5} + R_0^{3-k} + R_0^{3k+3}} R_1, \\
c_2 &= \frac{k\left(-(k+1)R_0^{2k} + kR_0^{2k+2} - 1\right)}{k^2 R_0^{k+1} - 2\left(k^2 - 1\right) R_0^{k+3} + k^2 R_0^{k+5} + R_0^{3-k} + R_0^{3k+3}} R_1, \\
c_3 &= -\frac{k\left(k\left(R_0^2 - 1\right) + R_0^2\left(R_0^{2k} + 1\right)\right)}{k^2 R_0^{k+1} - 2\left(k^2 - 1\right) R_0^{k+3} + k^2 R_0^{k+5} + R_0^{3-k} + R_0^{3k+3}} R_1, \\
c_4 &= \frac{k\left(kR_0^{2k} - (k-1)R_0^{2k+2} + R_0^2\right)}{k^2 R_0^{k+1} - 2\left(k^2 - 1\right) R_0^{k+3} + k^2 R_0^{k+5} + R_0^{3-k} + R_0^{3k+3}} R_1.
\end{aligned}
\tag{A 1}
$$

REFERENCES

Bassis, Jeremy N., Fricker, Helen A., Coleman, Richard & Minster, Jean-Bernard 2008 An investigation into the forces that drive ice-shelf rift propagation on the Amery Ice Shelf, East Antarctica. *J. Geology* **54** (184), 17–27.

Borstad, C., McGrath, D. & Pope, A. 2017 Fracture propagation and stability of ice shelves governed by ice shelf heterogeneity. *Geophys. Res. Lett.* **44** (9), 4186–4194.

Cardoso, S.S.S. & Woods, A. W. 1995 The formation of drops through viscous instability. *J. Fluid Mech.* **289**, 351–378.

Coussot, P. 1999 Saffman-Taylor instability in yield-stress fluids. *J. Fluid Mech.* **380**, 363–376.

Dallaston, M. C. & Hewitt, I. J. 2014 Free-boundary models of a meltwater conduit. *Phys. Fluids* **26** (8), 083101.

Doake, C. S. M. & Vaughan, D. G. 1991 Rapid disintegration of the Wordie Ice Shelf in response to atmospheric warming. *Nature* **350** (6316), 328–330.

Glen, J. W. 1955 The creep of polycrystalline ice. *Proc. R. Soc. A* **228** (1175), 519–538.

Holdsworth, G. 1983 Dynamics of Erebus Glacier tongue. *Ann. Glaciol.* **3**, 131–137.

Holloway, K. E. & de Bruyn, J. R. 2005 Viscous fingering with a single fluid. *Canadian Journal Of Physics* **83** (5), 551–564.

Homsy, G. M. 1987 Viscous fingering in porous-media. *Ann. Rev. Fluid Mech.* **19**, 271–311.

Hughes, T. 1983 On the disintegration of ice shelves: the role of fracture. *J. Glaciol.* **29** (101), 98–117.

Jha, Birendra, Cueto-Felgueroso, Luis & Juanes, Ruben 2011 Fluid Mixing from Viscous Fingering. *Phys. Rev. Lett.* **106** (19).

Kondic, L, Shelley, MJ & Palffy-Muhoray, P 1998 Non-Newtonian Hele-Shaw flow and the Saffman-Taylor instability. *Phys. Rev. Lett.* **80** (7), 1433–1436.

Lindner, A, Bonn, D & Meunier, J 2000*a* Viscous fingering in a shear-thinning fluid. *Phys. Fluids* **12** (2), 256–261.

Lindner, A., Coussot, P. & Bonn, D. 2000*b* Viscous fingering in a yield stress fluid. *Phys. Rev. Lett.* **85** (2), 314–317.

Manickam, O & Homsy, G. M. 1993 Stability of miscible displacements in porous-media with nonmonotonic viscosity profiles. *Physics of Fluids A-Fluid Dynamics* **5** (6), 1356–1367.

Mascia, S., Patel, M. J., Rough, S. L., Martin, P. J. & Wilson, D. I. 2006 Liquid phase migration in the extrusion and squeezing of microcrystalline cellulose pastes. *European journal of Pharmaceutical Sciences* **29** (1), 22–34.

Paterson, L. 1981 Radial fingering in a Hele Shaw cell. *J. Fluid Mech.* **113**, 513–529.

Paterson, L. 1985 Fingering with miscible fluids in a hele shaw cell. *Phys. Fluids* **28** (1), 26–30.

Pegler, S. S. & Worster, M. G. 2012 Dynamics of a viscous layer flowing radially over an inviscid ocean. *J. Fluid Mech.* **696** (-1), 152–174.

Roussel, N., Lanos, C. & Toutou, Z. 2006 Identification of bingham fluid flow parameters using a simple squeeze test. *J. Non Newt. Fluid Mech.* **135** (1), 1–7.

Saffman, P. G. & Taylor, G. 1958 The Penetration of a Fluid into a Porous Medium or Hele-Shaw Cell Containing a More Viscous Liquid. In *Proc. R. Soc. A*, pp. 312–329.

Sayag, R. & Worster, M. G. 2013 Axisymmetric gravity currents of power-law fluids over a rigid horizontal surface. *J. Fluid Mech.* **716**, 716 R5–1–716 R5–11.

Sayag, R. & Worster, M. G. 2019 Instability of extensional flows. part i: Experimental analysis. *J. Fluid Mech. Sub judice* .

Vandenberghe, N., Vermorel, R. & Villermaux, E. 2013 Star-Shaped Crack Pattern of Broken Windows. *Phys. Rev. Lett.* **110** (17).

Vermorel, R., Vandenberghe, N. & Villermaux, E. 2010 Radial Cracks in Perforated Thin Sheets. *Phys. Rev. Lett.* **104** (17).

Wooding, R. A. & Morelseytoux, H. J. 1976 Multiphase fluid-flow through porous-media. *Ann. Rev. Fluid Mech.* **8**, 233–274.

Zhao, H. & Maher, J. V. 1993 Associating-polymer effects in a Hele-Shaw experiment. *Phys. Rev. E* **47** (6), 4278–4283.